



**UNIVERSIDAD DE INVESTIGACIÓN DE
TECNOLOGÍA EXPERIMENTAL YACHAY**

Escuela de Ciencias Físicas y Nanotecnología

TÍTULO: Study of Sagittarius A* X-ray Spectra Flares

Trabajo de integración curricular presentado como requisito para la
obtención del título de Físico

Autor:

Pablo Daniel Contreras Guerra

Tutor:

José Manuel Ramírez Velásquez

Urcuquí, agosto 2019

Urququí, 20 de agosto de 2019

SECRETARÍA GENERAL
(Vicerrectorado Académico/Cancillería)
ESCUELA DE CIENCIAS FÍSICAS Y NANOTECNOLOGÍA
CARRERA DE FÍSICA
ACTA DE DEFENSA No. UITEY-PHY-2019-00003-AD

En la ciudad de San Miguel de Urququí, Provincia de Imbabura, a los 20 días del mes de agosto de 2019, a las 10:00 horas, en el Aula Sala Capitular de la Universidad de Investigación de Tecnología Experimental Yachay y ante el Tribunal Calificador, integrado por los docentes:

Presidente Tribunal de Defensa	CONTRERAS HERRADA, ERNESTO JOSÉ
Miembro No Tutor	ROJAS CELY CLARA INES
Tutor	RAMÍREZ JOSÉ MANUEL

Se presenta el(la) señor(ita) estudiante CONTRERAS GUERRA, PABLO DANIEL, con cédula de identidad No. 1725158065, de la ESCUELA DE CIENCIAS FÍSICAS Y NANOTECNOLOGÍA, de la Carrera de FÍSICA, aprobada por el Consejo de Educación Superior (CES), mediante Resolución RPC-SO-39-No.456-2014, con el objeto de rendir la sustentación de su trabajo de titulación denominado: *Study of Sagittarius A*X-ray Spectra Flares*, previa a la obtención del título de FÍSICO/A.

El citado trabajo de titulación, fue debidamente aprobado por el(los) docente(s):

Tutor RAMÍREZ JOSÉ MANUEL

Y recibió las observaciones de los otros miembros del Tribunal Calificador, las mismas que han sido incorporadas por el(la) estudiante.


Previamente cumplidos los requisitos legales y reglamentarios, el trabajo de titulación fue sustentado por el(la) estudiante y examinado por los miembros del Tribunal Calificador. Escuchada la sustentación del trabajo de titulación, que integró la exposición de el(la) estudiante sobre el contenido de la misma y las preguntas formuladas por los miembros del Tribunal, se califica la sustentación del trabajo de titulación con las siguientes calificaciones:

Tipo	Docente	Calificación
Tutor	RAMÍREZ JOSÉ MANUEL	9,9
Presidente Tribunal De Defensa	CONTRERAS HERRADA, ERNESTO JOSÉ	10,0
Miembro Tribunal De Defensa	ROJAS CELY CLARA INES	9,9

Lo que da un promedio de: 9.9 (Nueve punto Nueve), sobre 10 (diez), equivalente a: **APROBADO**


Para constancia de lo actuado, firman los miembros del Tribunal Calificador, el/la estudiante y el/la secretario ad-hoc.


CONTRERAS GUERRA, PABLO DANIEL
Estudiante


CONTRERAS HERRADA, ERNESTO JOSÉ
Presidente Tribunal de Defensa


RAMÍREZ JOSÉ MANUEL
Tutor


ROJAS CELY CLARA INES
Miembro No Tutor

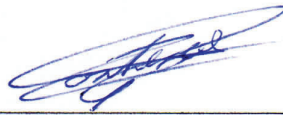


CIFUENTES TAFUR, EVELYN CAROLINA
Secretario Ad-hoc

AUTORÍA

Yo, **PABLO DANIEL CONTRERAS GUERRA**, con cédula de identidad 1725158065, declaro que las ideas, juicios, valoraciones, interpretaciones, consultas bibliográficas, definiciones y conceptualizaciones expuestas en el presente trabajo; así cómo, los procedimientos y herramientas utilizadas en la investigación, son de absoluta responsabilidad de el/la autora (a) del trabajo de integración curricular. Así mismo, me acojo a los reglamentos internos de la Universidad de Investigación de Tecnología Experimental Yachay.

Urcuquí, agosto de 2019.



Pablo Daniel Contreras Guerra
CI: 1725158065

AUTORIZACIÓN DE PUBLICACIÓN

Yo, **PABLO DANIEL CONTRERAS GUERRA**, con cédula de identidad 1725158065, cedo a la Universidad de Tecnología Experimental Yachay, los derechos de publicación de la presente obra, sin que deba haber un reconocimiento económico por este concepto. Declaro además que el texto del presente trabajo de titulación no podrá ser cedido a ninguna empresa editorial para su publicación u otros fines, sin contar previamente con la autorización escrita de la Universidad.

Asimismo, autorizo a la Universidad que realice la digitalización y publicación de este trabajo de integración curricular en el repositorio virtual, de conformidad a lo dispuesto en el Art. 144 de la Ley Orgánica de Educación Superior

Urcuquí, agosto de 2019.



Pablo Daniel Contreras Guerra
CI: 1725158065

Agradecimiento

Esta tesis representa la culminación de una gran etapa en mis estudios y preparación profesional y me gustaría reconocer a todos los que de una forma u otra me han ayudado y han sido mi apoyo durante estos años:

En primer lugar, quiero agradecer a José Manuel Ramírez, mi tutor de tesis y quien me introdujo en una rama tan fascinante de la física: la astronomía de rayos X. Gracias al tema elegido, aprendí mucho sobre las técnicas y habilidades necesarias para investigar en este campo y, en particular, aprendí mucho sobre la naturaleza fascinante de nuestro centro galáctico.

Los resultados informados en este trabajo se basan en observaciones realizadas por el Observatorio de rayos X Chandra. Además, este trabajo ha utilizado el software proporcionado por el Centro de rayos X Chandra (CXC) en los paquetes de aplicación CIAO, ChIPS y Sherpa. Me gustaría reconocer la misión tan importante, impresionante y líder en investigación que es Chandra.

Gracias también a todas las personas que forman parte de Yachay. Aprecio mucho ser parte de este proyecto. Todos los profesionales, grandes profesores e investigadores que he conocido han contribuido y me han inspirado para tener una perspectiva y objetivos completamente nuevos en mi vida. Yachay, y toda su gente, representa un gran paso en mi carrera profesional y espero seguir contribuyendo a un proyecto tan grande.

Mi vida universitaria no sería una experiencia tan increíble y llena de buenos recuerdos sin todos los amigos que he adquirido. No solo han estado conmigo en momentos de tiempo libre y relajación, sino que han sido de ayuda y apoyo a través de los diferentes desafíos en la universidad. Me enorgullece decir que juntos hemos tenido éxito y espero que continuemos teniendo éxito en nuestra formación y vida profesional. Son varios, pero haré todo lo posible para no omitir a alguien; dicho esto, muchas gracias a: Ronny, Alexito, Pepe, Eva, Rafa, Willa, Mateín, Eri, Kabir, Osiris, Marlon, Mafer, Karlita, Magno, David, Álex, Rosita y finalmente, con un valor extra de cariño, Emilia.

Más importante aún, no llegaría tan lejos sin la ayuda y el apoyo interminable de mi familia. Gracias a mis queridos e incansables padres, Pablo Contreras y Mónica Guerra, que me han enseñado todas las cosas valiosas de la vida y que han sido el mayor ejemplo de amor, trabajo duro y unidad. Mi padre, Pablo, el hombre más inteligente que conozco y mi mejor ejemplo de compromiso, trabajo y amor. Mi madre, Mónica, la madre incansable y que siempre me apoya porque es llena de amor y sabios consejos. Gracias a mis primeros y mejores amigos desde siempre, mis hermanos: Andrés: mi ejemplo de coraje, María Reneé: mi ejemplo de voluntad, David: mi ejemplo de fortaleza, Mónica: mi ejemplo de pura amistad, y Juan: mi ejemplo de trabajo duro y de conseguir tus sueños. Ser parte de una familia tan grande ha sido la mayor bendición y, sobre todo, mi familia ha sido el mejor equipo de apoyo para mantenerme de pie frente a todo lo que quiera darme de baja. Definitivamente, mi hogar es mi lugar de descanso y tener a mis padres y hermanos juntos y cada vez que lo necesito es una fuente inagotable de fortaleza.

Para finalizar esta sección de agradecimientos, gracias a Dios, quien guió mi vida y me permitió ser parte de Yachay, estudiar Física y conocer gente maravillosa e inspiradora en el camino.

Resumen

Este trabajo presenta un estudio de rayos X de la variabilidad de emisión de Sagitario A* (Sgr A*) en observaciones de Chandra durante los años 2001 a 2017. Sgr A* es una fuente de radio compacta en el centro de la Vía Láctea con fuerte evidencia de ser un agujero negro supermasivo con una masa de $\sim 4 \times 10^6 M_{\odot}$. Sgr A* y el Centro Galáctico son el mejor laboratorio para estudiar los fenómenos de alta energía de los núcleos galácticos, ya que es el núcleo galáctico más cercano (~ 8 kpc) que permite observaciones de alta resolución. Las numerosas observaciones hacia el Centro Galáctico han revelado una emisión bastante débil ($\sim 10^{39}$ erg/s) proveniente de Sgr A* con una alta variabilidad; particularmente en la banda de rayos X que muestra actividades de llamarada. Específicamente, se construyeron mapas de flujo de la región central galáctica para ver la variabilidad de las emisiones y su correlación con estructuras mayores como nubes moleculares. Particularmente, los mapas de flujo construidos en tres períodos diferentes mostraron estructuras similares de nubes moleculares encontradas en estudios anteriores y la variabilidad de emisión de rayos X es evidente como patrones de iluminación en los mapas. Dicha variabilidad se visualiza mejor si los tres mapas de flujo se unen en un mapa RGB que mostró variaciones complejas dentro de las nubes moleculares. Además, se realizó un análisis espectral para modelar la emisión del Centro Galáctico y caracterizarla con la variabilidad de la línea Fe K α . Esta línea es una prueba importante de fenómenos de alta energía y es una característica frecuente de las diferentes emisiones del centro galáctico. Los espectros se extrajeron de la vecindad inmediata de Sgr A*. Específicamente, los espectros correspondientes a los años 2012 y 2014 mostraron una característica interesante de un retraso en la variabilidad de la emisión de fondo y la emisión de la línea Fe K α . Tal comportamiento coincide con la interpretación de la emisión de la línea Fe K α como emisión reprocesada de fluorescencia en nubes de gas que rodean Sgr A*. A partir de los espectros analizados, la variabilidad de emisión de rayos X es nuevamente evidente. Sin embargo, la mezcla de observaciones de imagen y de espectroscopía de Chandra dio como resultado raros mapas de flujo de la región central galáctica presentes en mosaicos de flujo y pérdida en la resolución espectroscópica que impidió hacer fuertes aseveraciones con respecto a llamaradas presentes en la variabilidad observada.

Keywords: rayos X, Sgr A*, Fe K α , mapas de flujo, espectros.

Abstract

This work presents an X-ray study of the Sagittarius A* (Sgr A*) emission variability on Chandra observations data during the years 2001 to 2017. Sgr A* is a compact radio source at the center of the Milky Way with strong evidence to be a supermassive black hole with a mass about $\sim 4 \times 10^6 M_{\odot}$. Sgr A* and the Galactic Center are the best laboratory to study galactic nuclei high-energy phenomena as it is the closest (~ 8 kpc) galactic nucleus allowing high resolution observation runs. Extensive observations towards the Galactic Center have revealed a rather faint emission ($\sim 10^{39}$ erg/s) coming from Sgr A* with a particular high variability on the X-ray band showing flaring activity. Specifically, flux maps of the galactic central region were constructed to see the emission variability and its correlation to greater structures such as molecular clouds. Particularly, the flux maps constructed on three different periods showed similar structures of molecular clouds found on previous works and the X-ray emission variability is evident as illumination patterns on the maps. Such variability is better visualized if the three flux maps are put together on an RGB map which showed complex variations within molecular clouds. Additionally, spectral analysis was performed to model the Galactic Center emission and characterize it with the Fe K α line variability. This line is an important probe of high-energy phenomena and it is a prevalent feature of different galactic center emission. The spectra were extracted from the region in the immediate vicinity of Sgr A*. Specifically, spectra corresponding to the years 2012 and 2014 showed an interesting characteristic of a delay on the variability of the background emission and the Fe K α line emission. Such behavior is coincident with the interpretation of the Fe K α line emission as reprocessed, fluorescence, emission on gas clouds surrounding Sgr A*. From the analyzed spectra, X-ray emission variability is again evident. However, the mixing of Chandra imaging and spectroscopic data resulted on rare artifacts present on flux mosaics and loss on spectroscopic resolution preventing from doing strong asseverations regarding flaring periods on the seen variability.

Keywords: X-ray, Sgr A*, Fe K α , flux mosaics, spectra.

Contents

List of Figures	viii
List of Tables	ix
1 Introduction	1
1.1 X-ray Astronomy	1
1.1.1 X-rays	1
1.1.2 History	2
1.1.3 Fe $K\alpha$ Line	3
1.2 Sagittarius A* & the Galactic Center	4
1.2.1 Sagittarius A*	4
1.2.2 The Galactic Center	5
1.2.3 High Energy Emission	5
1.2.4 Accretion and Luminosity	6
1.3 The Chandra X-ray Observatory	7
1.3.1 Spacecraft	8
1.3.2 Mirrors	8
1.3.3 Gratings	11
1.3.4 Science Instrument Module	12
1.3.5 PCAD System	15
1.4 Motivation	16
1.4.1 Problem Statement	16
1.4.2 General & Specific Objectives	16
2 Methodology	17
2.1 Software	17
2.2 Data Retrieval	17
2.3 Data Reduction and Calibration	18

2.3.1	The Event File	18
2.3.2	Looking at the Data.....	20
2.3.3	Selecting Events of Interest	20
2.3.4	Extraction of Analysis Products	21
2.3.5	Calibration	22
2.4	Image Analysis.....	22
2.4.1	Contraction of R for Images	22
2.4.2	Flux Mosaics.....	24
2.5	Spectroscopy	24
2.5.1	Contraction of R for Spectra	24
2.5.2	Basics of Spectral Fitting	25
2.5.3	Software Implementation of Spectral Fitting	26
2.6	Lightcurves	28
3	Results & Discussion	31
3.1	Methodology	31
3.2	Flux Mosaics of the Central Region	38
3.3	Spectral Analysis.....	40
4	Conclusions & Outlook	45
A	Introduction to Chandra Data Products	47
A.1	ObsID Directory.....	47
A.2	Primary Directory.....	48
A.3	Secondary Directory.....	49
B	<code>celldetect</code> & <code>deflare</code>, visualization example	51
	Bibliography	53

List of Figures

1.1	Observatory Sketch	9
1.2	Incident X-ray on media	9
1.3	HRMA schematic	10
1.4	Rowland Geometry and Transmission Gratings	12
1.5	Science Instrument Module in the focal plane.....	13
1.6	ACIS instrument.....	13
1.7	HRC instrument.....	14
1.8	Lissajous-pattern	15
2.1	Fitting Process.....	26
3.1	Fe $K\alpha$ Mosaic Maps.....	38
3.2	RGB Map	39
3.3	Emission Spectra 2002-2006	41
3.4	Emission Spectra 2008-2011	41
3.5	Emission Spectra 2012-2014	42
3.6	Emission Spectra 2016-2017	42
B.1	Celldetect regions.....	51
B.2	Lightcurve and deflare GTI	52

List of Tables

1.1	Fluorescent emission lines.....	4
1.2	Sgr A* mass accretion rate.....	8
3.1	List of observations, part I.....	32
3.2	List of observations, part II.....	33
3.3	Spectral fitting results.....	40

Chapter 1

Introduction

1.1 X-ray Astronomy

1.1.1 X-rays

X-rays were first documented in 1895 by Wilhelm Conrad Röntgen*¹ though first discovered by Ivan Pulyui in 1880². Both investigated with cathode ray tubes and presented pictures of different body parts revealing internal bone structure. The discovery was attributed to Röntgen who named the novel form of radiation as X-rays, to indicate that it was unknown. X-rays are electromagnetic waves with much higher frequency, ν , than visible light, often defined as photons with energies between ≈ 0.1 keV and 512 keV (1 keV = 1.6×10^{-16} J). Such photons have wavelengths in the Ångström regime ($1\text{Å} = 10^{-10}\text{m}$) according to

$$E = h\nu = \frac{hc}{\lambda} \approx \frac{12.4\text{keV}}{\lambda/\text{Å}}. \quad (1.1)$$

The first described X-rays were produced as bremsstrahlung radiation from the electron beam being stopped at the anode end of the tube (accelerated charges produce electromagnetic radiation). But, X-ray photons can also be produced as radiation from very hot objects with 10^7 K, e.g. from astrophysical sources, or via inverse Compton-scattering of low energy photons off hot electrons³. Then, detection of X-ray from astrophysical sources is another way of looking and studying the universe. However, X-rays cannot be detected on ground-based telescopes as Earth's atmosphere shields most of X-ray radiation⁴. Therefore, to observe X-rays from the sky, detectors must be flying above Earth's atmosphere.

*Awarded with the first Nobel prize in 1901 "in recognition of the extraordinary services he has rendered by the discovery of the remarkable rays subsequently named after him" (http://nobelprize.org/nobel_prizes/physics/laureates/1901)

1.1.2 History

X-ray astronomy began at the end of World War II with military rockets repurposed to lift radiation detectors above the atmosphere for a few minutes at a time⁵. These first flights detected X-ray emission from the Sun. The first rocket flight to detect the first X-ray source beyond the solar system was on 1962, a source later found to be the brightest non-solar X-ray source, Sco X-1. This latter flight also detected a uniform X-ray background. Following flights with better spatial resolution and optical lenses identified Sco X-1 to be an X-ray binary with a compact (neutron) primary^{5,3}. After this success, further rocket flights were performed and more X-ray binaries, X-ray emission from supernova remnants, the radio galaxies M87 and Cygnus-A, and the Coma cluster were discovered⁵.

The first satellite X-ray was Uhuru, launched on 1970 and represented a big improvement as in its first day it exceeded the combined observation time of all previous X-ray astronomy experiments^{5,3}. It detected over 300 individual sources among pulsation of X-ray binaries and emission from clusters of galaxies. More X-ray satellite experiments followed on the 1970s, among them were Copernicus, Ariel-V (from UK), ANS (from the Netherlands), OSO-8, and HEAO-1⁵. These missions found more classes of astronomical X-ray sources, more time variability on X-ray binaries and detected first iron emission lines. The next revolutionary X-ray experiment was Einstein Observatory launched in 1979 by the National Aeronautics and Space Administration (NASA), which provided the first true X-ray images. Einstein combined an X-ray telescope and an imaging proportional counter providing the sensitivity (more than 2 orders higher than missions before) to observe large samples of stars, binaries, galaxies, cluster of galaxies and active galactic nuclei (AGN)^{5,3}.

The 1980s were a period of progress for Europe and Japan in X-ray astronomy. In 1983, the European Space Agency (ESA) launched the European X-ray Observatory SATellite, EXOSAT, launched into a deep 90-hour period orbit allowing long and continuous observations. The Japanese scientific space agency, ISAS, followed a program to place proportional and scintillation counters on the satellites: Hakucho, Tenma and Ginga. In this decade quasi-periodic oscillations (QPOs) in X-ray binaries, iron emission and absorption lines from AGN and iron emission lines from the Galactic center were discovered^{5,3}. The ROentgen SATellite, ROSAT, was launched on 1990 by a German-UK-US collaboration. It had an X-ray and extreme ultraviolet (EUV) telescopes and performed the first all-sky survey generating a catalog with more than 150 000 objects⁵.

The next big step in X-ray astronomy was the implementation of X-ray sensitive charged-coupled devices (CCDs) providing better imaging and spectroscopic properties than previous imaging proportional counters and scintillators⁵. ASCA was the first X-ray mission implementing CCDs, launched in 1993 by a collaboration between NASA and ISAS⁵. It also implemented low-weight optics on an extendable structure giving a long enough focal length for detection up to 10 keV, including the important 6-7 keV iron line region. This allowed the detection of relativistic broadened iron lines in black hole accretion disks and the broad energy band detection allowed the discovery of non-thermal emission of supernova remnants⁵. NASA launched the Rossi X-ray Timing Explorer, RXTE, on 1995^{5,3}. It was designed to collect many events from bright sources and examine their variability down to microsecond scales monitoring them from day to year timescales. New discoveries were spin periods in low-mass X-ray binaries and kilohertz QPOs⁵.

Great observatories represent the current state of X-ray astronomy. The Chandra X-ray Observatory from NASA was launched on 1999⁶. Its most important quality is its sub-arc second resolution telescope that gives high-resolution

images and spectra in the range 0.1 keV to 10 keV. Its elliptical high-earth orbit allows for long observations^{6,3}. The European X-ray Multi Mirror satellite XMM-Newton from ESA was launched at the end of 1999³. It has the largest collecting area than any focusing X-ray telescope making it the most suitable to do spectroscopy with weaker sources³. It also includes optics that allows detection of light in the range 180 to 650 nm. Suzaku from Japan Aerospace Exploration Agency (JAXA) was launched on 2005 on a low-Earth orbit^{5,3}. It has a wider energy band (10 - 600 keV) and lowest background. It also included the first X-ray micro-calorimeter on a satellite giving the best energy resolution but due to a flaw it stopped working³.

Further missions of X-ray astronomy can be mentioned, however, it would make an unnecessarily longer history introduction. For detailed information on X-ray astronomy introduction, history and technical details on the instruments and further considerations on X-ray astronomy the reader can see Keith Arnaud⁵, Giacconi *et al.*⁷, Hanke³, Charles and Fabian⁸.

1.1.3 Fe K α Line

The X-ray waveband contains atomic and ionic transition signatures for nearly all astronomically abundant elements⁵. These correspond to transitions involving electrons in the 1s shell primarily, although, for heavier atoms (i.e. Fe, Ni), transitions can involve higher shells as well. Particularly strong transitions include the ones from hydrogen-like and helium-like ions, ions with more electrons like strong lines from Fe XVII through Fe XXIV, as well as fluorescent transitions from neutral or low ionized atoms. Here the latter will be discussed with particular emphasis on the characteristic Fe K α transition line. More information on the mentioned strong transitions can be found on the Appendix 1 in Keith Arnaud⁵ and further atomic data useful for X-ray astronomy can be found at <http://www.atomdb.org> or in the *X-ray Data Booklet*[†].

Fluorescent emission lines can arise when an atom or ion has an inner-shell electron removed possibly by photoionization, accelerated particle collision, or nuclear transition. After this, the ion becomes very unstable and will rapidly fill the electron "hole" with an electron from a less-bound shell. This process releases energy that can further ionize the ion or be emitted as a "fluorescent" photon⁵. The relative probability of further ionization vs. fluorescence depends primarily on the nuclear charge; low-Z elements tend to ionize, iron with a K-shell hole has a $\sim 30\%$ chance of emitting a photon and elements much heavier than iron tend towards fluorescence⁵. Fluorescence is described first by the shell of the electron hole, so that "Fe K" line refers to a transition ending with an electron moving to the K-shell. In addition, to point out the energy difference of the transition (i.e. Δn) Greek letters are used; e.g. α denotes a transition from $n = 2$ to $n = 1$ and β denotes a transition from $n = 3$ to $n = 1$. Further information about the orbital angular momentum of the electrons can be given with integer subscripts with values incrementing by 1. **Then, a Fe K α transition line is produced by removing a K-shell electron by X-ray photoionization or by collisional ionization by accelerated particles, and then quickly filling the vacancy by an electron from the L-shell**^{5,9,10}. Table 1.1 shows the fluorescent emission lines from common astrophysical elements.

The Fe K α line at 6.4 keV from neutral or low-ionized plasma is of particular interest because it is an important probe of high-energy phenomena in various astrophysical sites. The Fe K α line emitted from a hot, thermally-ionized

[†]<http://xdb.lbl.org>

Element	$K\alpha_1$	$K\alpha_2$	$K\beta_1$	$L\alpha$	$L\beta$
C	0.277				
N	0.3924				
O	0.5249				
Ne	0.8486	0.8486			
Na	1.0410	1.0410	1.0711		
Mg	1.2536	1.2536	1.3022		
Al	1.4867	1.4863	1.5575		
Si	1.7400	1.7394	1.8359		
S	2.3078	2.3066	2.4640		
Ar	2.9577	2.9556	3.1905		
Ca	3.6917	3.6881	4.0127	0.3416	
Fe	6.4038	6.3908	6.4905	0.6374	0.6488
Ni	7.4782	7.4609	8.2647	0.8515	0.8588

Table 1.1: Fluorescent emission lines (in keV), from Krause and Oliver¹¹.

plasma at ionization equilibrium is generally in the range 6.6-6.7 keV depending on the plasma temperature¹⁰. This emission line is a prevalent feature in the X-ray spectra of AGN. It is present also in spectra from X-ray binaries. In such objects, the line is attributed to fluorescence from photoionized matter in the vicinity of the compact X-ray source. This line is also detected in solar flares, low-mass flaring stars, massive stars, young stellar objects, supernova remnants and molecular clouds in the Galactic center region¹⁰.

This characteristic emission has been widely studied in the case of the Sun. Observed line intensity and light curve during several flares had suggested that the excitation of Fe atom electrons occur mainly by photoionization induced by X-ray flares with a probable additional contribution from collisional ionization¹⁰.

1.2 Sagittarius A* & the Galactic Center

1.2.1 Sagittarius A*

The center of our galaxy, The Milky Way, is our closest galactic nuclei and it is at the heart of scientific interest as it is the best laboratory to study phenomena and physical processes that may occur in the center of other galaxies as well. It hosts the compact radio source Sagittarius A* (Sgr A*), located within a dense stellar cluster surrounded by a small cluster of high velocity stars and several components of neutral, ionized and extremely hot gas^{12,13}. The closeness of Sgr A* makes possible to have numerous observations with high sensitivity and resolution along 18 orders of magnitude in energy of electromagnetic radiation¹². Simultaneously, theoretical simulations, with increasing power, have been performed to explain these observations¹². Altogether these studies on the orbits of high velocity stars of the central cluster and on the radiation from the galactic center, have given strong evidence to associate the compact

radio source with a supermassive black hole (SMBH) with mass of $\sim 4.3 \pm 0.3 \times 10^6 M_{\odot}^{\ddagger}$ and at a distance of only $\sim 8 \text{ kpc}^{\S 14 12 13}$.

1.2.2 The Galactic Center

The central region of The Milky Way hosts a dense and luminous star cluster and several components of neutral, ionized and extremely hot gas^{15 12 16}. In particular, the central parsec consists of a mostly ionized HII region, "the Sgr A West", additional to a concentration of X-ray emitting gas at $\sim 10^6 \text{ K}^{17 18 19 20 12}$. This central cavity is filled with a set of orbiting filaments of ionized gas - the "mini spiral" in Lo and Claussen²¹. Surrounding this region, dense molecular clouds orbiting at $R \sim 1.5 - 4 \text{ pc}$ form the "circum-nuclear disk"^{22 23 12}. Surrounding this region there is a number of molecular clouds of 5 – 100 pc scales and the young supernova remnant, "Sgr A East"^{15 12}.

There is a stellar cluster with an inward increasing density from a scale of tens of parsecs to the central parsec^{24 12}. The compact radio source Sgr A* is at the center of this cluster. Its intrinsic size is of 3 – 10 light minutes, determined by Very Long Baseline Interferometry (VLBI) observations at centimeter and millimeter wavelengths^{25 26 27 28}. Sgr A* has a faint emission at all the bands excepting the radio to submillimeter region, thus matching the radio source to be a SMBH may seem unconvincing at first. Strong evidence to confirm Sgr A* as a SMBH was established with precise determination of stellar orbits within $\sim 0.02 \text{ pc}$ from the radio source¹². Given its proximity, high-resolution observations are possible with much more detail and specific information than any other galaxy nucleus. The resolution goes up to a linear scale comparable to the radius of Earth's orbit around the Sun¹². Particularly, the Galactic Center can be observed in long-wavelength bands from infrared to radio, and in short wavelength bands from X-rays to γ -rays. However, the Galactic Center is obscured in the optical region by thick dust^{24 29}.

1.2.3 High Energy Emission

The central region contains several components of diffuse, hard X-ray line and continuum emission with temperatures around 10^7 to 10^8 K ($1 - 10 \text{ keV}$)^{20 12}. The 6.4 keV neutral Fe K α line and the X-ray continuum show strong spatial correlation with large molecular clouds on scales of 10 – 30 pc in the central region^{30 31 12}. This component is attributed to a Compton reflection/fluorescence of cold gas irradiated by time variable hard X-ray continuum sources, very likely to be Sgr A*^{9 32 12}.

In more extended scales, the continuum and highly ionized Fe 6.7 keV line emission may be attributed to diffuse gas or many unresolved point sources^{20 12}. Observations have supported a diffuse X-ray emission of distributed plasma with a range of temperatures^{33 34 12}. A soft, truly-diffuse emission fits with a thermal plasma with a temperature of $kT \sim 1 \text{ keV}$ showing spatial structures at arcminute or smaller scales resulting from stellar winds interacting with other stellar winds or stellar winds and supernova remnants with cold and ionized gas^{20 19 12 35 29}. At higher temperatures ($kT \sim 7.5 \text{ keV}$), the plasma is spatially more uniform but broadly correlated with the softer component. Its thermal diffuse emission comes from resolved and unresolved accreting magnetic white dwarfs^{20 36 29}. Regarding the hard X-ray continuum emission, it is associated with a superposition of unidentified compact sources, likely to

[‡]Black Hole masses are given in solar masses $M_{\odot} = 1.98 \times 10^{30} \text{ kg}$

[§]1 pc = 3.2616 ly = $3.0857 \times 10^{16} \text{ m}$

be cataclysmic variable stars (CVs)^{20 32 37 12 29}. Observations on such extended scales have resolved > 80% of the $\sim 6 - 7$ keV line and continuum emission into discrete sources making a strong case for compact stellar sources interpretation^{38 12}.

The central parsec presents a diffuse emission consistent with thermal emission from a $kT \sim 1$ keV plasma and electron density of $\sim 30f^{-1/2}\text{cm}^{-3}$, with f the emission filling factor, i.e. the fraction of the volume that is occupied by emitting gas³⁹. Additionally there is the compact source associated with Sgr A* itself and other compact stellar sources as well. Finally, the X-ray emission in Sgr A West is connected to more extended emission from the entire Sgr A complex and the supernova remnant Sgr A East.

1.2.4 Accretion and Luminosity

Sgr A* is most of the time in a steady, quiescent state punctuated by flaring activity, specially at X-rays, while the surrounding molecular clouds carry evidence of much violent X-ray outbursts in the past^{12 29 13}. It is a remarkably under-luminous black hole, i.e. emitting at $L \sim 10^{36}$ erg/s[¶] its luminosity is by more than eight orders lower compared to its Eddington limit, i.e. the maximum luminosity a body can achieve, ($L_{Edd} \sim 1.5 \times 10^{41} L_{\odot}$ for Sgr A*) and more than four orders below the luminosity estimated from the accretion at the Bondi radius[¶]. Such luminosity is dominated by accretion from stellar winds in Sgr A* vicinity. Larger accretion rates may occur from low angular momentum gas clouds falling into the center or star scattering within the tidal disruption radius ($R_t \sim 10R_S$)^{40 12}.

Steady Emission from Sgr A*

The compact radio source is detectable at all times showing moderate flux and spectral variations^{41 42 43 44 12}. Particularly, steady and faint X-ray emission is also detected. The steady state X-ray emission, including 6 – 7 keV Fe K line emissions, is $L \sim 2 \times 10^{33}$ erg/s following a soft power-law spectrum^{45 19 12}. Different theoretical models with radiatively inefficient accretion flows have been proposed to explain the faintness of Sgr A* emission. Advection dominated accretion flow (ADAF in Narayan *et al.*⁴⁶) models explain low luminosity by the combination of high ratio of tangential gas velocities with hot protons and cold electrons decoupling in low density gas. However, observational discrepancies ruled out the model and led to a convection dominated accretion flow (CDAF in Ball *et al.*⁴⁷, Narayan *et al.*⁴⁸ and Quataert and Gruzinov⁴⁹) models. They incorporate lower accretion rates and shallower density profiles. Later sets of models are radiative inefficient accretion flow models with substantial mass loss (RIAFs in Yuan *et al.*⁵⁰), advection-dominated inflow-outflow solutions (ADIOS in Blandford and Begelman⁵¹) and jet models⁵². For spectral modeling, hybrid models involving thermal and non-thermal components are used. In general, the faint quiescent emission of the X-ray band is explained by thermal Bremsstrahlung in the transition between ambient medium and accretion zone^{53 45 12}.

[¶]1 erg = 10^{-7} J

[¶]The Bondi radius comes from setting the escape velocity equal to the sound speed.

Variable emission from Sgr A*

Sgr A* emission is variable at all wavelengths with very different degree of variation at different energy bands¹². Particularly, the largest variations are seen in the X-ray band, orders above longer wavelengths variability, in which the luminosity can increase by a factor up to a few hundreds. The brightest flare observed so far is about 160 times brighter than the steady state⁵⁴. At low fluxes, X-ray variability is still unknown.

Flares

Key issues in the emission variability is to discriminate if it corresponds to statistical fluctuations or flare events with distinct properties¹². The brightest observed flare had a luminosity of $L \sim 3.9 \times 10^{35}$ erg/s and the spectrum follows a power-law, compatible with the quiescent state but slightly harder^{54 19}. Available data are inconclusive on whether X-ray lightcurves exhibiting flares have quasi-periodic oscillations. During a typical flare, the X-ray flux has been observed to increase by factors few to tens suggesting that the electron energy distribution in flares is distinct that in the quiescent state and not just an increase on the quiescent distribution¹².

The physics of the flare emission are not certain as the quiescent state. The proposed models for X-ray flares are: synchrotron radiation from higher energetic electrons^{50 55}, synchrotron self-Compton emission, inverse Compton emission^{56 57 58} or combinations of these²⁹. From the observations and modeling it can be concluded that X-ray flares could result from the acceleration of a small fraction of the particle distribution in the innermost accretion zone. The possible reason is magnetic reconnection and conversion of magnetic energy into the energy density of relativistic particles^{59 55 60}.

Regarding the geometry of the flares, few constrains are given by the emission processes and physical conditions of the flare. Three plausible scenarios are a jet with blobs of ejected material, hot spots orbiting the SMBH and statistical fluctuations in the accretion flow¹².

Accretion

The faintness of Sgr A* is surprising given the rich gas reservoir in its immediate surroundings. It can be understood from the drastic decrease of effective mass accretion towards the black hole¹². An overview of this decrease is shown in table 1.2. The physical origin for such low accretion and radiation efficiency is attributed to inefficient angular momentum transport at all radii, relatively poor coupling between electrons and protons at low gas densities, characteristic for Sgr A*, and strong outflows and convection in the innermost accretion zone^{51 49 59 61 60 62 12}.

1.3 The Chandra X-ray Observatory

X-ray features of the Galactic center and particularly of Sgr A* can only be seen with space telescopes. This section presents an overview of the Chandra X-ray Observatory (CXO), which performed the observations for the data retrieved and used in this work. The CXO combines an efficient high-resolution ($\leq 1/2$ arcsec) X-ray telescope with a suite of advanced imaging and spectroscopic instruments. It is the X-ray component of NASA's four Great

	Radius [pc, R_S]	Mass [M_\odot]	Mass accretion rate [M_\odot/yr]
Molecular clouds	10 - few 100 pc	$10^{5.5} - 10^{6.5}$	10^{-2}
Circum-nuclear disk	1.7 - 7 pc	a few $10^4 - 10^5$	$10^{-3} - 10^{-4}$
Central cavity, mini spiral & stellar cluster	< 1.7 pc	a few 10^2	$10^{-3} - 10^{-4}$
Stellar winds at Bondi radius	0.05 pc = $10^5 R_S$		a few 10^{-6}
Outer accretion zone	$10^2 - 10^3 R_S$		< 10^{-6}
Inner accretion zone	a few $\cdot 10^2 R_S$		a few $10^{-9} - 10^{-7}$

Table 1.2: Overview of mass and accretion rate as function of the distance from the SMBH. It is clear the increasing inefficiency of the accretion rate as matter comes closer to Sgr A*. Retrieved from Genzel *et al.*¹²

Observatories along with the Hubble Space Telescope, the Compton Gamma-Ray Observatory and the Spitzer Space Telescope⁶. It was designed to provide order-of-magnitude advances over previous X-ray astronomy missions with regards to spatial and spectral resolution. The dissertation work from Hanke³ has a nicely done introduction to the observatory and its facilities, therefore this section will follow its structure.

1.3.1 Spacecraft

Originally called the *Advanced X-ray Astrophysics Facility (AXAF)* the observatory was renamed after the Indian astronomer Subrahmanyan Chandrasekhar **. NASA's satellite Chandra, with a mass of 4.8 tons, was launched by the Space Shuttle Columbia on 1999, July 23. Subsequently an Inertial Upper Stage and Chandra's Internal Propulsion System placed the observatory in a high elliptical orbit⁶. As of December 2017, the apogee height, after a period of decreasing since 2012, reached a minimum of $\sim 129,000$ km; the perigee, after increasing since 2012, reached a maximum of $\sim 19,000$ km. The orbital eccentricity reached its minimum of ~ 0.68 in December, 2017. Now the trend inverted to an increasing apogee and decreasing perigee and the eccentricity is estimated to reach a maximum of ~ 0.91 by ~ 2024 . The orbit allows for high observing efficiency by spending most of the time above the radiation belts ($\sim 75\%$) and long observations (currently ~ 170 ksec) are possible by the orbital period of 63.5h⁶. However, limitations on observation times arise due to thermal considerations, see CXC⁶ for more information.

The Observatory carries several high precision instruments as illustrated on Fig. 1.1, the most important ones will be introduced in the following subsections. For an extensive description of these instruments and all the information corresponding Chandra, please refer to the Proposer's Observatory Guide (CXC⁶).

1.3.2 Mirrors

CXO's unique capability largely relies on its High Resolution Mirror Assembly (HRMA). For a comprehensive description of HRMA it is helpful to discuss first the deflection of X-rays. X-rays incident on a material will, in

**Chandrasekhar (1910-1995) won the Nobel prize in 1983 "for his theoretical studies of the processes of importance to the structure and evolution of the stars" (http://nobelprize.org/nobel_prizes/physics/laureates/1901)

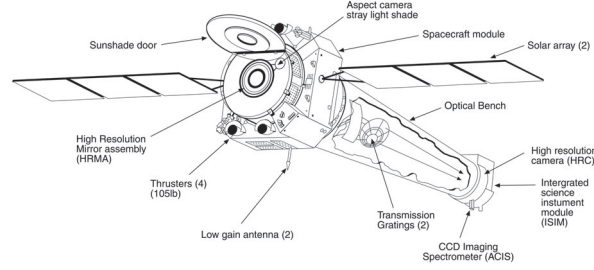


Figure 1.1: Sketch of the Chandra X-ray Observatory with some subsystems labeled. Retrieved from CXC⁶

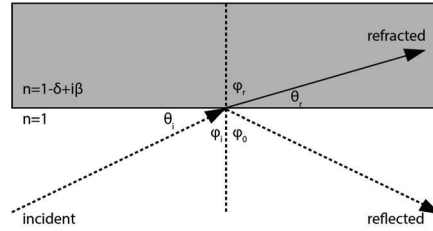


Figure 1.2: An X-ray from the vacuum impacts a medium at a grazing angle θ_i . If $1 - \delta$, the real part of the refraction index, is less than 1, the refracted angle θ_r will be less than the grazing angle. For total reflection, the grazing angle must be less than $\arctan(1 - \delta)$ ⁵.

general, penetrate or be absorbed, therefore, its usage in medical diagnosis and so³. Deflection is only possible by total reflection if X-rays graze a mirror surface with small angles (typically less than 1 degree). The interaction between an incident ray in vacuum and a solid medium is shown in Fig. 1.2. The medium has an index of refraction $n = 1 - \delta + i\beta$, with δ and β optical constants. In the X-ray regime, both constants are much smaller than unity (they are proportional to the square of the wavelength). When the medium is conductive, β is non-zero and the refracted ray will decay exponentially. Incident and refracted angles are related by Snell's law:

$$\sin\phi_r = \frac{\sin\phi_i}{(1 - \delta)}. \quad (1.2)$$

In X-ray optics, it is conventional to use the grazing angle $\theta = \pi/2 - \phi$ measured relative to the tangent to the surface. Snell's law is then:

$$\cos\theta_r = \frac{\cos\theta_i}{(1 - \delta)}. \quad (1.3)$$

Total reflection occurs when there is no real solution for θ_r in (1.3). Since $\cos\theta_r$ cannot exceed unity, there is a critical grazing angle below which is impossible for refraction to happen and total reflection occurs. The angle is given by, $1 = \cos\theta_c = \cos\theta_i / (1 - \delta)$.

For small angles, $1 - \delta = \cos\theta_c \approx 1 - \theta_c^2/2$ and thus $\theta_c \approx \sqrt{2\delta}$.

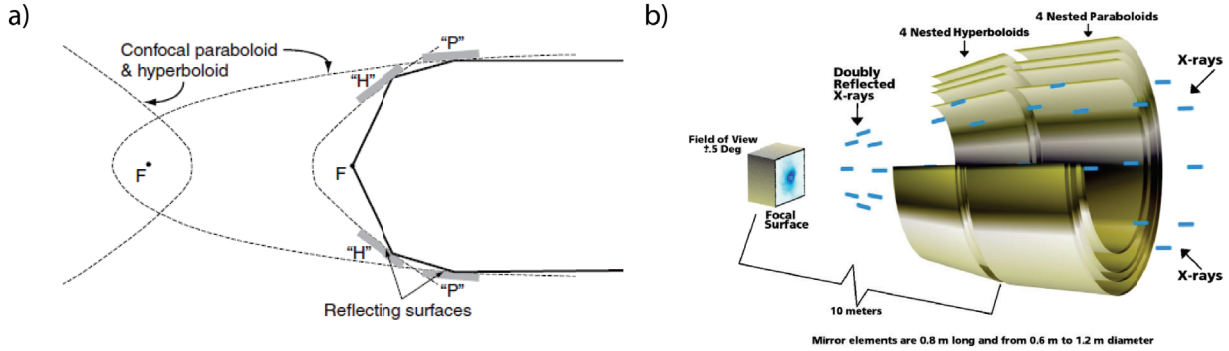


Figure 1.3: *a)* Schematic of a Wolter type I mirror, taken from Keith Arnaud⁵. *b)* Schematic of the HRMA. The total reflection and convergence of incoming X-rays is shown. Retrieved from CXC⁶

At X-ray energies, E , the optical constant δ is given by:

$$\delta = \frac{r_e (hc/E)^2 N_e}{2\pi} \quad (1.4)$$

where r_e is the classical electron radius, N_e the electron density, h the Planck's constant and c the speed of light. since N_e is proportional to the atomic number Z , it follows that:

$$\theta_c \propto \frac{\sqrt{Z}}{E} \quad (1.5)$$

Therefore, the critical angle decreases with energy and higher Z materials are favorable for the reflecting surface⁵.

HRMA is a Wolter I-type⁶³ mirror system. It is a nested set of four paraboloid-hyperboloid grazing incidence X-ray mirror pairs. Wolter⁶³ on his work proved that two reflections are needed to form an image over a finite field of view (FOV) and considered the possible conic geometries to achieve the image. The principle is that to achieve perfect imaging, the optical path must be identical for all incident rays on the telescope⁵ and derived three possible geometries. In types I and II, X-rays first reflect off the concave surface of a paraboloid and then of the concave or convex surface of a hyperboloid. In type III, is first a reflection off the convex paraboloid surface and later the reflection from the concave surface of an ellipsoid.

A scheme of the geometry of type I mirror is shown in figure 1.3. It is the most useful mirror for X-ray astronomy as it gives the largest aperture-to-focal length ratio. This ratio is key discriminant in maximizing the collecting area while staying within severe dimensional restrictions. Wolter type I mirror gives an effective aperture area of $2\pi R\alpha l$ (l is the mirror length), since α is small, a set of mirrors with different radii R_i should be nested to give a larger area for intercepting X-rays⁵. In CXO's case, HRMA (see figure 1.3) consists of four nested Wolter type I mirrors with outer diameters of 1.23, 0.99, 0.87 and 0.65 m⁶. As the critical angle scales with \sqrt{Z} (Eq. 1.5), heavy metals are favorable, thus a 33 nm thick iridium layer was deposited on the surface of the mirrors. HRMA's geometric aperture is 1145 cm², however, the final effective area is lower and energy dependent (Eq. 1.5) and there are many other considerations, see Keith Arnaud⁵ chapter 1 for a more extensive introduction on X-ray optics and CXC⁶ for the

specific Chandra implementation. Furthermore, it has been a 2.2 nm contamination layer of hydrocarbons on the mirror affecting the efficiency of the telescope. The focal length of the mirror system is ~ 10 m and the HRMA's weight is 1484 kg⁶.

1.3.3 Gratings

Chandra can be used for both imaging or spectroscopy⁶. The two modes are realized by transmission gratings that can be either stay tilted or be flipped into the optical path. In the latter case producing dispersed images following the grating diffraction relation, $m\lambda = p\sin\theta$, where m is the integer order number, λ the photon wavelength, p the spatial period of grating lines and θ the dispersion angle. A "normal" undispersed image is formed by the zeroth-order events, $m = 0$, and dispersed images are formed by higher orders, primarily the the first-order, $|m| = 1$ ³.

There are two systems of transmission gratings on CXO, the Low and High Energy Transmission Gratings (LETG and HETG). Both consist of Rowland gratings, i.e. grating facets are mounted on a toroidal aluminum assembly. This geometry assures that photons being diffracted from the different facets are focused again to the same point, thus reducing optical aberration³. The Rowland circle is the intersection of the torus with the plane in the direction of dispersion and perpendicular to the focal plane, see figure 1.4. It contains the the mirror's focal point and also all focal points of the Rowland grating. The Rowland spacing is 8.63 m (\approx diameter of the circle)⁶.

While the ACIS-S detector (cf. 1.3.4) is placed tangentially to the circle for use with the HETG, parts of the HRC-S detector (cf. 1.3.4), for use with the LETG, are tilted to follow the circle, as low energies lead to larger deflection such that the curvature of the Rowland circle becomes more important³.

LETGS

When inserted behind HRMA, the LETG diffracts X-rays into a dispersed spectrum. It uses 0.5 μm thick gold wires with 1 μm period as its grating. Support structures in perpendicular and triangular directions with 25 μm and 2 mm period produce additional diffraction, see figure 1.4. Together with the HRMA and HRC (cf. 1.3.4), the Low Energy Transmission Grating Spectrometer (LETGS) provides high spectral resolutions of $\Delta E/E = 1000$ in the low energy range 0.08 - 0.2 keV⁶.

HETG

The HETG is used for higher energies, 0.4-10 keV, with also a high resolution of $\Delta E/E = 1000$. It comprises two grating systems: the High and Medium Energy Gratings (HEG and MEG). In both systems, the grating facets are made by gold bars of specific periods. HEG and MEG differ by 10° in their dispersion direction thus forming a X on the image of a point source. HEG occupies the inner two rings of the Rowland torus with 144 grating facets with gold bars of 1200 \AA width and 2001 \AA period on thin polyimide substrate, see figure 1.4. In the case of MEG, occupying the outer two rings, it consists of 192 facets with 2080 \AA width and 4002 \AA period. This almost 2:1 ratio of period and width suppresses dispersion in even orders⁶.

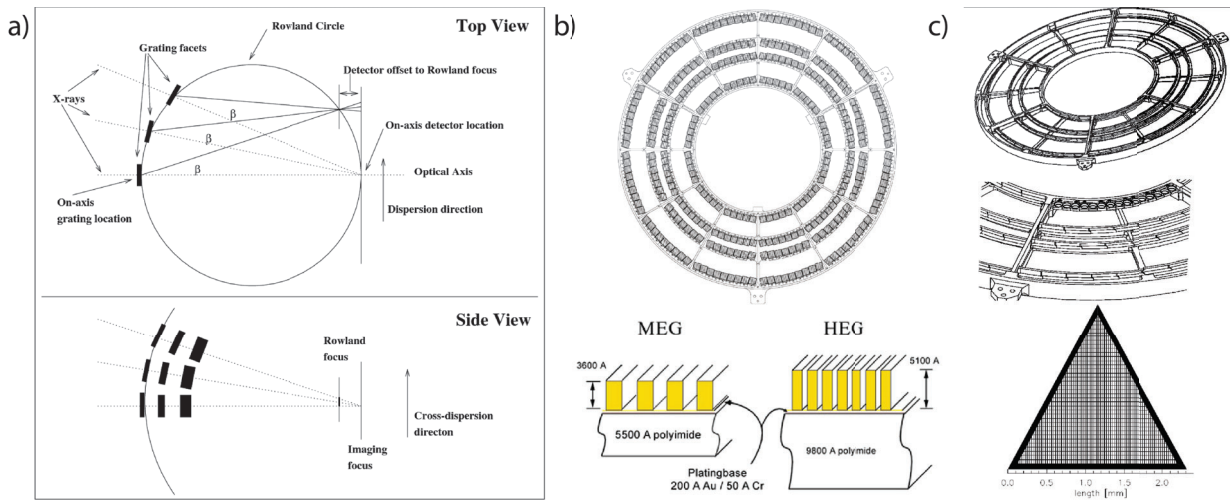


Figure 1.4: *a)* Rowland geometry scheme. The "Top" view is across the dispersion direction. The geometry is such that rays being diffracted at specific angle β by the gratings (on the Rowland circle) converge on a point also in the Rowland circle. Dotted lines are zeroth order and solid lines are first-order rays. The "Side" view is along the dispersion direction. This shows the astigmatic nature of the spectrally focused image; as the converging rays don't reach yet the imaging focus, they are extended across the dispersion. *b)* HETG scheme. At the top is shown the support structure of the HETG, it applies the Rowland curvature. At the bottom it is shown the cross section of the MEG and HEG membranes which are mounted and the grating facets. *c)* LETG scheme. At the top it is the support structure of the LETG. At the middle, grating modules mounted on the structure. At the bottom, the triangular structure supporting the grating gold wires mounted on the rings on the modules. All the sketches presented in this figure were retrieved from CXC⁶

Implemented together with HRMA and ACIS (cf. 1.3.4) it forms the High energy Transmission Energy Spectrometer (HETGS). HEG has a larger spectral resolution (5.5\AA per ACIS detector pixel) while MEG (with 11\AA per pixel) covers a larger range of wavelengths⁶.

1.3.4 Science Instrument Module

The Science Instrument Module (SIM) consists of special hardware providing mechanical and thermal interfaces to the focal-plane scientific instruments. Its most important functions are the capability to adjust the telescope focal length and the ability to move the instruments along a direction orthogonal to the optical axis⁶. The SIM contains the two focal instruments - the Advanced CCD Imaging Spectrometer (ACIS) and the High Resolution Camera (HRC). Each with two principal components a longish one for grating spectroscopy (-S) and a square shaped for imaging analysis (-I). The SIM moves in the X-axis for focusing and in the Z-axis for instrument and aimpoint selection. A scheme of the focal plane instrument is shown in figure 1.5.

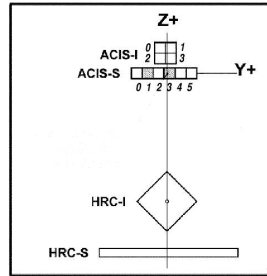


Figure 1.5: Arrangement of the ACIS and HRC instruments in the focal plane. SIM motion can be used to place the aimpoint at any point on the vertical line. The view is along the telescope axis from the mirrors. Retrieved from CXC⁶.

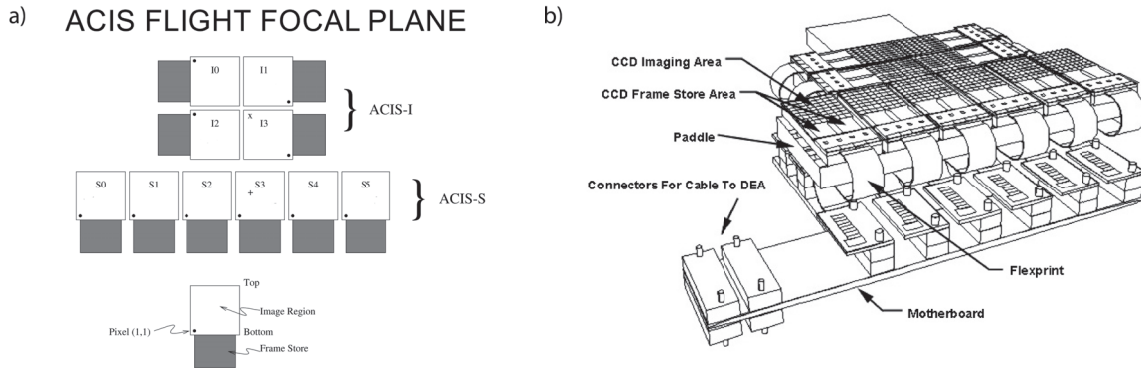


Figure 1.6: a) Layout of the ACIS chips on the focal plane. b) Schematic of the ACIS instrument with labeling of the different components. Retrieved from CXC⁶.

ACIS

The ACIS consists of four ACIS-I (in a 2×2 array) and six ACIS-S (1×6 array) CCD chips, see figure 1.6. At most 6 chips can be used simultaneously in various configurations. For imaging purposes, the default chips are I0-I3 and S2-S3, but also the configuration S1-S4, I2-I3 could be used. In spectroscopy-mode the used chips are S0-S5⁶.

Each CCD is a silicon solid-state detector with 1024×1024 pixels, each of $24 \mu\text{m}$. The ACIS detector works at -90 to -120 °C to avoid the electrons to be excited to the conduction band via thermal excitation, but via inner photo effect i.e. absorbed X-rays produce a large number of electron-hole pairs³. The produced charge is measured and proportional to the X-ray energy, one pair is produced for each 3.7 eV. Contrasting with an optical CCD in which roughly one electron is excited by each photon and the number of electrons is proportional to the intensity of light³. Visible light is blocked by optical blocking filters, thick layers ($\approx 3.5 \mu\text{m}$) of aluminum and polyimide above the CCD chips³.

There are two type of CCD chips in use; most of them, with the exception of two chips, are front illuminated

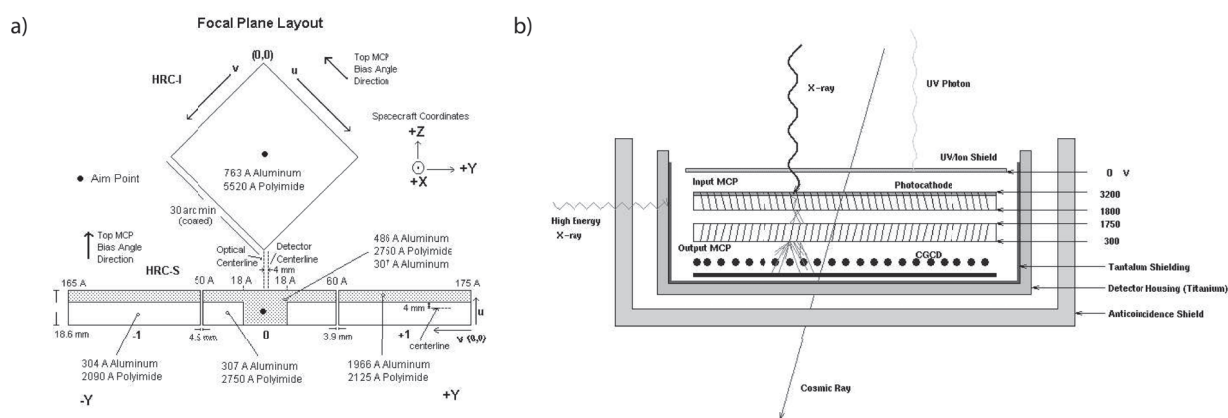


Figure 1.7: *a)* Layout of HRC on the focal plane with labeling on materials, dimension and so. *b)* Schematic view of the HRC module components and the interaction of X-rays, UV light and cosmic rays with it. Note the tilting of the MCP tubes. Retrieved from CXC⁶.

(FI) and the other two are back-side illuminated (BI)⁶. FI chips store the charges and read them on the front side, therefore, the electronics exposed to radiation. For this, the FI chips suffered damage from radiation since the beginning of the mission: high-energy protons, not sufficiently shielded, are focused just like X-ray by the mirrors during early passages through radiation belts³. After this was realized, the detector is removed from the mirror's focal plane when the observatory is passing through the belts⁶. S1 and S3 chips are BI, i.e. the charges are generated and read out on the back side of the chip, possible because X-rays can penetrate the silicon crystal³. ACIS efficiency has decreased slowly but continuously due to molecular (mainly carbon) contamination on optical blocking filters.

The CCDs have an "active" or imaging section which is exposed to the incident radiation and a shielded "frame store" region⁶. The mode of the ACIS CCD readout is: (1) the active region is exposed to radiation for a fixed time (~ 3.2 s); (2) after the exposure, the excited charges in the active region are quickly (~ 41 ms) transferred in parallel into the frame store; (3) next exposure begins; (4) simultaneously, the data in the frame store is transferred in serial to a local processor which identifies position and amplitude of any events according to some criteria⁶. The position and amount of collected charge, together with similar data for the region containing and surrounding the pixel are classified and passed to the telemetry system⁶.

HRC

The High Resolution Camera (HRC) is a microchannel plate (MCP) instrument comprised of two detectors, one optimized for imaging (HRC-I) and the other for spectroscopy (HRC-S), which is the read out of the LETG (cf. 1.3.3). HRC-I provides the largest field-of-view ($\sim 30' \times 30'$) aboard Chandra and its sensitivity is higher than that of ACIS, though without comparable spectral resolution. The time resolution is also the best in the observatory ($\sim 16 \mu\text{sec}$), but it is only used under some considerations (see Section 7.11 on CXC⁶). An scheme of the HRC is shown in figure 1.3.4.

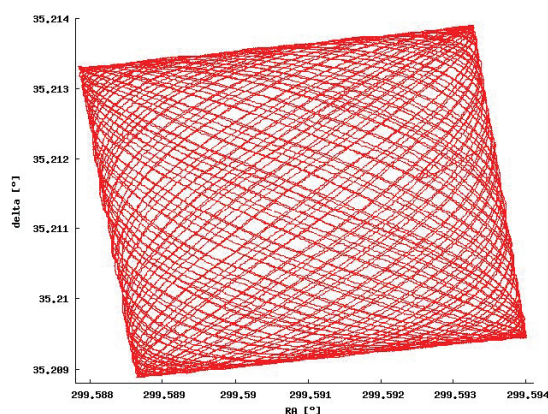


Figure 1.8: The Lissajous pattern applied by Chandra's PCAD system to avoid information loss and reduce bad pixel effects³.

In the HRC, X-rays first enter through a UV/ion shield, necessary to avoid (ideally) signals from UV light, ions or low energy electrons. Then the rays are absorbed in the CsI walls of the first (input) of two consecutive MCPs⁶. The axes of the tubes comprising the input and output MCPs are not parallel to the optical axis but tilted at 6° in opposite directions (see figure 1.3.4) to improve probability of interaction. CsI coating enhances photoemission. The resulting photoelectrons are then accelerated by an applied electric field. The next interaction with the MCP releases several secondary electrons and so on, generating a cascade of electrons⁶. The second MCP provides additional gain and reversing the direction of the tilt angle reduces the possibility of ion feedback^{††}. The electron cloud emerging from the output MCP is accelerated to a position-sensitive charge detector. The X-ray position is then determined by calculating the centroid of the produced charge cloud via the "three tap algorithm" (see section 7.2 of CXC⁶).

1.3.5 PCAD System

If the target of the ACIS would be focused steadily there would be information loss as the ACIS detector has gaps of 18 pixels between the chips⁶. Chandra, however, dithers in a Lissajous-pattern (see figure 1.8) spreading the image over several detector pixels. This also reduces the effect of bad pixels. Each single photon event is collected with a time-stamp allowing an easy reconstruction of the true image by post-observational data processing⁶.

The dithering is achieved by the pointing control and aspect determination (PCAD) system. It carries both propulsion systems to orientate the CXO and detector instruments to measure the actual orientation precisely⁶. This measurement is done by the aspect camera array (ACA) including a 11.2 cm optical telescope and CCD-cameras with as $1.4^\circ \times 1.4^\circ$ FOV, and two inertial reference units with several gyroscopes⁶.

^{††}Opposite direction moving ions can cause release of electrons starting the process again.

1.4 Motivation

1.4.1 Problem Statement

Sgr A* keeps being at the heart of scientific research as it is the closest SMBH and the best laboratory to observe very high energy phenomena happening on the universe. Furthermore, the observations and study on the Milky Way Galactic Center could be related with other Galactic nuclei showing similar emission properties. As discussed before, the Sgr A* case is very intriguing by its low luminosity and the physics underlying such behavior. Tracking its emission variability can give hints of past flares or an overall higher past activity. Although in longer wavelengths the steady emission and variable emission has been well described, at the X-ray band it is still under debate considerations about physical origin of the flares and variability and best models to describe Sgr A* activity.

1.4.2 General & Specific Objectives

The general objective of this work is to recognize and visualize the X-ray emission variability and structures of the galactic center and Sgr A* from Chandra X-ray observations on the period 2001 to 2017.

In particular, X-ray molecular clouds structures will be recognized in basis on structures described on previous works^{64,65} and the emission variability will be recognized on spectra from the stellar cluster in the vicinity of Sgr A*.

Specifically, flux mosaics of the galactic central region help to visualize the molecular cloud structures and spectrum extraction and fitting give hints on the emission variability by means of the Fe K α line emission variability. Particularly, the model used for spectral fitting will serve as the probe of the physical processes underlying the characteristic emission.

Chapter 2

Methodology

Throughout this chapter a rather introductory description of the common methodology applied to analyze X-ray data from observations is presented. The raw data products coming from the satellite are introduced as well as the processes applied to them in order to obtain ready to analyze products. The specific analysis software packages for Chandra satellite data are also introduced. Finally, the basics of spectral fitting and its implementation is presented.

2.1 Software

The data analysis presented in this dissertation work has been done with CIAO. The Chandra Interactive Analysis of Observations, CIAO* is the software package developed by the Chandra X-Ray Center, CXC, for analyzing data from the Chandra X-ray Telescope⁶⁶. It contains the complete suite of mission-dependent tools and in the package distribution it is included a suite of powerful higher-level programs: for imaging analysis -SAOImage DS9⁶⁷, for spectral analysis -Sherpa⁶⁸ and CIAO's plotting platform -ChIPS; common tools needed for any analysis in X-ray Astronomy. CIAO can also be used for data from other missions, even non-X-ray missions. It is extensively documented on the CXC website[†] with many useful threads describing how to perform common analysis tasks.

2.2 Data Retrieval

Most of the data retrieved by Chandra observations, and other X-ray missions, is public and available online for the scientific community. It is also practical that X-ray astronomy data are concentrated in a small number of archives and it is clear where to retrieve data for a specific mission, i.e. Chandra.

Archives are extensive catalogs in which specific observations can be found. They have built-in search engines to find observations based on many categories: specific name, coordinates, year and so on. The observation data include

*from "s'sciavo", "I am a servant" in Venetian.

†<http://cxc.harvard.edu/ciao/index.html>

basic files, cleaned files and auxiliary information and the interface also allows to choose which files download for the selected observation.

In Chandra's case, the CXC is responsible for all satellite operations, including hosting of the Chandra archive. The CXC's WebChaSer[‡] is the interface which provides direct access to all Chandra's public data. Chandra's X-ray data can also be accessed via the HEASARC[§] repository, NASA's repository for X-ray, gamma-ray and cosmic microwave background data. It provides access to public data from all currently operating X-ray missions and all major past missions, for which data recovery was possible, as well; including US and non-US missions⁵. It hosts also catalogs for major astronomical missions operating in other wavebands.

An additional way to retrieve X-ray data from Chandra observations is via the command line on CIAO⁶⁶. With simple commands it is possible to search for particular observations and download all available data, or particular files from observations .

2.3 Data Reduction and Calibration

2.3.1 The Event File

X-ray detectors measure individual photons instead of integrated flux as instruments for longer wavelengths do. X-ray photons have large energies allowing to single photon detection and as they have relatively low fluxes, they are easy to count. Then, the basic data structure is a list of detected events with a set of attributes. Typically, these attributes are position on the detector, time of arrival and attributes related to energy⁵. In addition to these attributes, most lists also include other quantities to discriminate events from background and so. All X-ray astronomy data is stored in FITS (Flexible Image Transport System) format⁶⁹. It consists of an empty primary image extension required by the format standard followed by a binary table extension with the event list and then a number of subsidiary extensions containing information for analysis. Further information about the detector status is stored in auxiliary files. A list of the attributes for X-ray data in a Chandra ACIS event file and a list with description of the files included in the Chandra Data Products can be found in Appendix A. The raw attributes are not sufficient for scientific analysis so they are processed to create refined attributes⁵. This is usually done automatically by the mission data center, i.e. CXC for Chandra through the Standard Data Processing (SDP) pipeline⁶. The major steps are introduced bellow.

Calculation of sky position

The position of an event is that of the detector initially. For example, consider a detector consisting of an array of four CCDs. The raw detector position (something like "Event on CCD 3, position 431,617") is converted first to one in a coordinate system in the local plane ("Event at position 3183,2184")⁵. Such conversion requires knowledge on pixel size and orientation of the detector and usually it does not vary with time. The new position is the detector coordinates: DETX, DETY; named by convention and defined looking down on the focal plane from the sky⁵. Next, the conversion to sky coordinates requires knowledge of where the focal plane was pointing when the event

[‡]<https://cda.harvard.edu/chaser/>

[§]<https://heasarc.gsfc.nasa.gov/>

was detected. This information is supplied by the auxiliary star-tracker telescope, the PCAD system in the case of Chandra⁶. And, given the dithering effect introduced earlier, this conversion will be time-variable. The sky coordinates are calculated for a tangent plane approximation to the celestial sphere, with the normal direction of the plane defined as the nominal pointing direction of the observation (stored as keywords RA_NOM and DEC_NOM)⁵. The positions (X,Y) in the event file are in pixel units and can be converted to right ascension and declination in the World Coordinate System (WCS) keywords. An issue concerning Chandra is that the detector pixel sizes and spatial resolution are comparable. If all events were placed at the center of detector pixels, the resulting image would have a gridded appearance. This is solved using subpixel repositioning and reduces the effective pixel size by using event shapes⁷⁰.

Calculation of energy or wavelength

CCDs, as other non-dispersive spectrometers, accumulate charge for each X-ray detected. This charge is called pulse-height amplitude, PHA. The conversion between PHA and energy may not be linear and vary with time or position on the detector. Any variability is corrected and stored as PI, for PHA invariant⁵. The relation between PI and energy of the photon is in the response matrix, c.f. 2.5.1. In CCDs the X-ray can produce charge in not just one pixel but in the neighboring pixels too. So that charges from 3×3 pixel regions are stored in a vector, PHAS. The total charge of the event is then the sum of PHAS charges for those pixels which produced charge for a single event⁵. Dispersive spectrometers, such as Chandra's transmission gratings determine the wavelength from the dispersion distance between the zeroth order position (un-dispersed ray) and the position of the photon. As there is overlap between diffraction orders, the wavelength measure may not be unique. This degeneracy is broken when the detector has energy resolution, such as CCDs⁵.

Calculation of time

The event time is recorded on-board relative to the spacecraft clock. It is converted to a time at Earth and recorded in seconds relative to the modified Julian date (MJD)[¶] for the mission. Chandra has a MJD offset of 50814.0000 days⁵. Most of the time this conversion is enough, but for sources with high time variability or precise trajectory the time should be converted to Solar System barycenter to eliminate effects due to Earth's orbit. Such process is not done in the automatic processing because the precise information about the satellite orbit is not known yet when the processing is done. Missions carrying detectors like CCDs such as Chandra, accumulating events within a frame time and reading them out, need a rule to assign a time to the events within each frame. Chandra uses the middle of the frame⁶.

Non-X-ray Background Rejection

Energetic particles (cosmic rays) can interact with the detectors and create non-X-ray background. The signal often differs from an X-ray, e.g. they create a different pattern of charge on pixels. Rejecting this events improves

[¶]Julian date is the number of days since noon on January 1, 4713 BCE. MJD is Julian date - 2400000.5 days

the signal-to-noise ratio so that processing systems are set to reject types of events that are always background⁵. However, researchers have always the choice to remove even further background events with the chance to reject some true X-rays.

2.3.2 Looking at the Data

It is always recommended to look at the data in all the ways possible as the SDP could have not cleaned up all the artifacts that could appear. Further processing to apply the latest calibration to the data and research specific calibration and events rejection must be addressed. Typical attributes that should be addressed before analyzing the data are:

- **Background flares:** Chandra, having a deep orbit and spending most of the time outside Earth's magnetosphere, is vulnerable to particle storms from solar flares. Such flares can be recognized and rejected by making a time series of event rates. Excluding such times of background flares from the data will improve the signal-to-noise ratio.
- **Hot spots, bad rows, flickering pixels and afterglows:** Detectors have often electronic hot spots or bad rows which can produce apparent signals which are neither X-rays nor background events. Events from these regions may be excluded on-board the spacecraft or excluded during processing⁵. Chandra includes a list of these data in an extension of the event file, the `bpix1` file (see Appendix A). Also, CCDs can involve the so-called flickering pixels which are sporadic. For Chandra this is not an issue as it runs cold enough to not produce flickering pixels. Chandra has an additional effect in the ACIS instrument, a pixel showing a signal for a few contiguous frames (i.e. a few tens of seconds). This is named "afterglow" and is due to cosmic-ray interactions with the CCD. It can be removed using standard CIAO tools⁵.
- **Pileup:** Integrating detectors like CCDs are vulnerable to pileup when exposed to bright sources. Two photons hitting the detector in the same or adjacent pixels in a single frame will not be distinguished and will look like a single event with higher energy. This will cause either in rejecting both events or both events will appear as a single one with higher energy. This causes an image of a bright source with a hole in its center as events are rejected from pileup and the spectrum will also result distorted⁵.

2.3.3 Selecting Events of Interest

Further filtering is always necessary to select the events of interest for a particular research. There are many ways of doing so, for instance see Keith Arnaud⁵. Here is presented the three ways applied on this work.

- **By region:** Any instrument with spatial resolution will require spatial filtering on the region of interest. Region filters consist of a combination of individual shapes specifying whether the enclosed pixels are to be included or excluded⁵. They can be defined in many formats or even as an argument to a program. The two main formats are DS9/FUNTOOLS and CIAO formats, both formats can be produced intuitively on the graphical user interface, GUI, of SAOImage DS9⁶⁷. Also, DS9 provides several tools for defining the regions

and its attributes (e.g. centroid, shape, dimensions) specifically and it allows to save the region files in the formats mentioned above in either image, physical or WCS coordinates. Image coordinates are in pixels and can vary if the pixel binning is changed, therefore not recommended⁵. Physical coordinates are the values in the event file (e.g. X and Y for sky or DETX and DETY for the detector) and the WCS coordinates are the right ascension and declination in either decimal or sexagesimal format.

Spatial filtering through regions allows to fast and powerful analysis but the researcher should always check that the coordinates are the correct ones and that the region being selected does in fact enclose physically interesting objects.

- **By time interval:** Good time intervals, GTIs, are the time intervals in which events are accumulated⁵. Chandra's data has GTI extension for each detector. There is possible to provide additional GTI filters by command line or by GUI. For instance, GTIs can be defined to reject periods of high background flares.
- **By spectral channel:** When there is interest on analyzing a specific energy band, filtering on spectral channel should be used. It can be used also to improve the signal-to-noise ratio by filtering out the lowest and highest spectral channels as most instruments are less efficient at the limits of their bandpass^{5,6}. Background could also increase at low and high ends by electronic noise and energetic particles, respectively⁵. There is no fixed recommendation on which channels should be rejected, mostly it depends on the particular interests of the research.

2.3.4 Extraction of Analysis Products

Most analysis tools do not work on the event file but on byproducts. Such byproducts can be thought as a projection of a multidimensional space of the event file onto one or two dimensions and then binning⁵. Thus, obtaining histograms of counts in one or two dimensions. Such histograms are:

- **Image:** Images typically are constructed from the X and Y columns in the event file. The detector coordinates, (DETX and DETY) could also be used to check detector artifacts⁵. Specially for Chandra, due to the PCAD system dithering, a point source will be smeared out on detector coordinates but in sky coordinates it will look clearly. Regarding the binning, a rule of thumb is to choose a bin size about one third of the full width at half maximum of the spatial resolution⁵. Non-standard images could be constructed by binning other columns. For example, TIME and PI (energy) columns could be binned to visualize spectral variability causing each pixel to have number of counts at particular time and energy⁵.
- **Spectrum:** Event file columns with information on energy are PHA and PI as noted earlier. The event file could contain an additional ENERGY column, derived from PI and the detector gain, which may be plotted just to have a quick estimate of the energies and some attributes like lines or edges⁵. It should not be used for scientific analysis. The spectrum is constructed from the PI column, always checking to have the latest calibration processing on the data. For non-imaging detectors, i.e. HETG or LETG, the automated processing often creates spectra^{5,6}. For imaging spectroscopy the source spectrum is likely to be extracted from a region and a background spectrum could be created from another source.

- **Lightcurve:** They are time series, constructed using the TIME column of the event file. It is important to notice that CCDs could produce periodic readouts on the lightcurves if the bin size is not a multiple of the frame time⁵. For instance, for a bin size of 1.5 frame times, alternate bins will contain one or two frames generating a spurious periodic signal.

2.3.5 Calibration

Processing in X-ray astronomy usually includes information about the detector during the analysis step using calibration files. Consider first an exposure producing observed counts $C(X, Y, PI)$ in a given channel and PI bin. These counts came from a source flux $S(X_S, Y_S, E, t)$ in photons/cm²/s/keV/arcmin² for a given position (X_S, Y_S) in the sky, at energy E and time t ⁵. S and C are related by:

$$C(X, Y, PI) = \int \int \int \int R(X, Y, PI, X_S, Y_S, E, t) \cdot S(X_S, Y_S, E, t) \cdot dX_S \cdot dY_S \cdot dE \cdot dt, \quad (2.1)$$

where R is the instrumental response in cm² in this definition. R provides a measure of the probability of a photon coming from (X_S, Y_S) with energy E at time t to be detected in the pixel (X, Y) and bin PI ⁵. Contractions of R lead to the products introduced before, the following section will consider such procedure for each product along with a further discussion regarding each analysis product.

2.4 Image Analysis

2.4.1 Contraction of R for Images

An image is created by summing over PI bins, therefore:

$$\begin{aligned} C(X, Y) &= \sum_{PI} C(X, Y, PI), \\ &= \int \int \int \int \left(\sum_{PI} R(X, Y, PI, X_S, Y_S, E, t) \right) \cdot S(X_S, Y_S, E, t) \cdot dX_S \cdot dY_S \cdot dE \cdot dt, \\ &= \int \int \int \int R_{image}(X, Y, PI, X_S, Y_S, E, t) \cdot S(X_S, Y_S, E, t) \cdot dX_S \cdot dY_S \cdot dE \cdot dt, \end{aligned} \quad (2.2)$$

where the instrumental response for images is:

$$R_{image}(X, Y, PI, X_S, Y_S, E, t) = \sum_{PI} R(X, Y, PI, X_S, Y_S, E, t). \quad (2.3)$$

It can be split into the point spread function (PSF), and effective area (EA), also called exposure map:

$$R_{image}(X, Y, PI, X_S, Y_S, E, t) = \text{PSF}(r, \theta, X_S, Y_S, E) \cdot \text{EA}(X_S, Y_S, E, t), \quad (2.4)$$

where $r^2 = (X - X_S)^2 + (Y - Y_S)^2$ and $\theta = \arctan[(Y - Y_S)/(X - X_S)]$. The PSF contains information about the spatial resolution of the telescope as a probability distribution of the event position on the detector from a point

source, i.e. it describes the shape and size of the image produced by a delta function^{5,6}. X-ray telescopes are often described to have a fixed resolution, e.g. $\sim 0.5''$ for Chandra, described on terms of the half-power diameter¹ but that is rather informal. Actually, the PSF is strongly energy-dependent and often position dependent also, degrading at higher energies and further from the optical axis⁵. Other considerations concerning the PSF arise such as not being azimuthally symmetric and radial lines caused by X-ray scattering. Then, the exact appearance of such effects is highly dependent on the mirror manufacture⁵.

The exposure map is the telescope area at (X_S, Y_S) given an X-ray with energy E at time t . It is time-dependent as near the edge of the detector a sky pixel may spend part of the time on the detector and part of it off the detector, because of the pointing dither, i.e. figure 1.8. Such effect is calculated using the telescope's "aspect history" which lists the pointing direction as a function of time⁵. Such information is provided as an auxiliary file on the data products (see Appendix A).

To produce a particular energy band image in photons/cm²/s/keV/arcmin² it is recalled the PSF as a δ -function⁶ and use:

$$\begin{aligned} C(X, Y) &= \int \int \int \int EA(X_S, Y_S, E, t) \cdot \delta(X_S - X) \cdot \delta(Y_S - Y) \cdot S(X_S, Y_S, E, t) \cdot dX_S \cdot dY_S \cdot dE \cdot dt, \\ &= \int \int EA(X_S, Y_S, E, t) \cdot S(X_S, Y_S, E, t) \cdot \Delta A \cdot dE \cdot dt, \end{aligned} \quad (2.5)$$

with ΔA the area of the pixel in arcmin². Assuming S to be constant and the image made for energy E_0 :

$$S(X, Y, E_0) = \frac{\left[\frac{C(X, Y)}{\Delta A} \right]}{\int EA(X, Y, E_0, t) \cdot dt}. \quad (2.6)$$

When the image is over wider energy bands it is necessary to assume that S can be split into position and energy dependent factors, i.e. $S = S_{im} S_{spec}$ where S_{spec} is determined in spectroscopic analysis⁵. Thus:

$$C(X, Y) = \int \int EA(X, Y, E, t) \cdot S_{im}(X, Y, t) \cdot S_{spec}(E, t) \cdot \Delta A \cdot dE \cdot dt. \quad (2.7)$$

Assuming again that S_{im} is not variable:

$$S_{im}(X, Y) = \frac{\left[\frac{C(X, Y)}{\Delta A} \right]}{\int \int EA(X, Y, t) \cdot S_{spec}(E, t) \cdot dE \cdot dt}. \quad (2.8)$$

A reasonable criteria is to apply the latter method when the central energy of the band divided by the width of the bandpass is less than $\sim 4^5$.

In addition, around 1.5-2 keV most X-ray telescopes show a strong variation in their effective areas by atomic edges in the reflecting surface, i.e. iridium for Chandra, so that particular attention should be given in such bandpass⁵. Further considerations regarding pileup or dead-time effects should be taken into account; for instance, see Keith Arnaud⁵ and CXCR⁶.

¹The diameter within which half of the focused X-rays are enclosed.

2.4.2 Flux Mosaics

It is common the case where a source emission is larger than the FOV. Therefore, multiple images must be mosaiced to cover such extended object. This operation has two steps; recast the raw-count images, effective area maps and background images to a common coordinate system, i.e. reproject the events to a common, specified grid, and then to combine all of the images in the same way that individual images would be constructed⁵. Making mosaics is a good test of the background removal producing obvious artifacts if there is error on the strength or distribution of backgrounds.

In low count rates, around one count per pixel, division of the raw count image by the exposure time enhances the values of individual pixels with low counts compared with higher counts regions. This results in a mosaic in which it is incapable to interpret properly the true variation in surface brightness by just seeing it. To target this, the mosaics are generally smoothed over areas large enough to include many counts⁵.

2.5 Spectroscopy

2.5.1 Contraction of R for Spectra

Spectra are created by binning over a region and assuming S does not vary within the region or in time.

$$C(PI) = \int \left(\int \int \int \int \int R(X, Y, PI, X_S, Y_S, E, t) \cdot dX_S \cdot dY_S \cdot dX \cdot dY \cdot dt \right) \cdot S_{spec}(E) \cdot dE. \quad (2.9)$$

The response R is split between a vector with units of cm^2 and a unitless matrix. The vector, stored in the Ancillary Response File (ARF), have information on the detector quantum efficiency and the matrix, called Redistribution Matrix Function, represents a normalized redistribution of the response file⁷¹. Equation 2.9 is reduced to

$$C(PI) = T \int \text{RMF}(PI, E) \cdot \text{ARF}(E) \cdot S_{spec}(E) \cdot dE, \quad (2.10)$$

where T is the total good observation time,

$$\text{RMF}(PI, E) = \int \int \int R_{\text{RMF}}(X, Y, PI, E, t) \cdot dX \cdot dY \cdot dt, \quad (2.11)$$

and

$$\text{ARF}(E) = \int \int \int \int \int R_{\text{ARF}}(X, Y, X_S, Y_S, E, t) \cdot dX_S \cdot dY_S \cdot dX \cdot dY \cdot dt. \quad (2.12)$$

If the source is diffuse and varies in surface brightness across the region then (2.11) can be modified to give a source-flux-weighted RMF.

$$\text{RMF}(PI, E) = \frac{\int \int \int S(X, Y) \cdot R_{\text{RMF}}(X, Y, PI, E, t) \cdot dX \cdot dY \cdot dt}{\int \int S(X, Y) \cdot dX \cdot dY}. \quad (2.13)$$

RMF gives the probability of a photon of given energy to be detected as a count in a particular bin in the spectrum. A theoretical perfect detector the matrix would be diagonal with each energy mapped on a single channel of the detector⁵. However, as expected, real detectors will always have some spread in their response.

The total response for energy E is:

$$\text{ARF}(E) \cdot \int \text{RMF}(PI, E) \cdot dPI. \quad (2.14)$$

And recalling the normalization of RMF:

$$\int \text{RMF}(PI, E) \cdot dPI = 1.0, \quad (2.15)$$

for all energies.

X-ray telescopes usually have PSFs with wide wings so a chosen source region may not include all the flux. Then, the ARF should be defined relative to the flux enclosed⁵.

2.5.2 Basics of Spectral Fitting

The grating spectrometers on Chandra do not obtain the actual spectrum of the source, but photon counts (C) within specific instrument channels (PI), i.e. ACIS or HRC. The observed spectrum is related to the actual spectrum of the source ($S_{spec}(E)$) by the relation in (2.10). It is ideal then to determine the actual spectrum of a source, by solving (2.10) for $S_{spec}(E)$, i.e. deriving $S_{spec}(E)$ for a set of $C(PI)$. Unfortunately, such inversions is not possible in general as they tend to be non-unique and unstable for small changes⁷¹.

Choosing a model spectrum, $M(E)$, that can be described in terms of a few parameters (i.e. $M(E, p_1, p_2, \dots)$), and matching it to the data obtained by the spectrometer is the usual alternative. The model should be chosen based on the physics of the source⁵. For each $M(E)$, a predicted count spectrum ($C_p(PI)$) is calculated and compared to the observed data ($C(PI)$). From the comparison a "fit statistic" is computed and used to decide whether the model spectrum "fits" the data obtained by the spectrometer. The model parameters are varied to find the values giving the best fit statistic. Such values are referred as the best-fit parameters and the model spectrum, ($M_b(E)$), made up from these parameters is considered the best-fit model⁷¹.

The most common fit statistic used to determine the "best-fit" model is χ^2 , defined as:

$$\chi^2 = \sum \frac{[C(PI) - C_p(PI)]^2}{[\sigma(PI)]^2}. \quad (2.16)$$

where $\sigma(PI)$ is the error of the channel PI , generally unknown but usually estimated by $\sqrt{C(PI)}$ ⁷¹.

Once a "best-fit" model is obtained, two questions must be addressed:

- How confident is that $C(PI)$ could have been produced by $M_b(E)$? The answer is known as the goodness of the fit criterion. The χ^2 statistic provides a criterion for a given number of degrees of freedom, ν (which is calculated as the number of channels minus the number of model parameters) and for a given confidence level⁷¹. When χ^2 exceeds critical tabulated values it can be concluded that $M_b(E)$ is not an adequate model

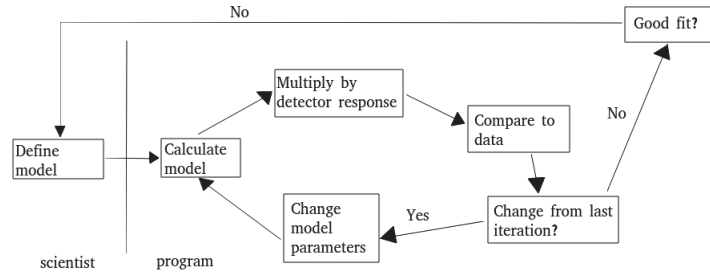


Figure 2.1: Schematic on the spectral fitting process.

$C(PI)$. A general rule is to have the "reduced χ^2 " ($\sim \chi^2/\nu$) approximately equal to one ($\chi^2 \sim \nu$)⁷¹. A reduced χ^2 much greater than one indicates a poor fit and one much less than one could indicate over-estimation of errors on the data. Even if $M_b(E)$ passes the goodness of the fit test, it may not be the only acceptable model. For data that is not good enough, there may be many different models with good fits.

- For a parameter, p_1 on the best-fit model, what is the range of values in which the true value of the parameter lies? This is known as the parameter "confidence interval". It is calculated by varying the parameter until χ^2 increases by a particular amount above the "best-fit" value⁷¹. The allowed amount to increase, the critical $\Delta\chi^2$, depends on the required confidence level and number of parameters whose space is being calculated.

2.5.3 Software Implementation of Spectral Fitting

The main components for spectral fitting mentioned above - observed spectra ($D(PI)$ for the source and $B(PI)$ for background), instrumental responses $RMF(PI, E)$ and $ARF(E)$, spectral models $M(E)$ - are implemented in the way described below. It is implemented in common spectral fitting software, such as XSPEC and Sherpa (the one distributed along CIAO and used in this work).

1. Choose the parameterized model thought to physically represent the actual spectrum of the source.
2. Choose the parameters values.
3. Predict the counts spectrum that would be detected by the instrument for the chosen model.
4. Compare the predicted to the observed counts spectrum.
5. Manipulate parameters until best fit between the theoretical model and observed data is found.
6. Calculate "goodness" of the fit and determine how well the model explains the observed data and calculate confidence intervals for the parameters.

The process is illustrated in figure 2.1. The following describes how Sherpa, with the implementation of XSPEC models, perform these tasks.

Observed Spectrum

Sherpa uses two files: the data file, containing the source spectrum $D(PI)$, and background file, containing $B(PI)$, although it also works with just the spectrum file. The spectrum file tells the software the photon counts detected in a given channel⁷¹. The background file is used to derive the background-subtracted spectra $C(PI)$ in counts per second given by:

$$C(PI) = \frac{D(PI)}{a_{D(PI)}t_D} - \frac{b_{D(PI)} B(PI)}{b_{B(PI)} a_{D(PI)}t_B}, \quad (2.17)$$

where $D(PI)$ and $B(PI)$ are counts in source and background; t_D and t_B are exposure times in background and data files; $a_{D(PI)}$ and $a_{B(PI)}$, $b_{D(PI)}$ and $b_{B(PI)}$ are area and background scaling values from source and background, together they refer the background flux to the same area as the observation as necessary⁵. This is the spectrum to which the XSPEC models are fitted by Sherpa.

Model Spectrum

The model spectrum is calculated using the same energy ranges in the response file with units of photons/cm²/s⁵. X-ray spectroscopic models are built up from individual components. These elements are of two types - additive (an emission component, like blackbody or spectral line) or multiplicative (something modifying the spectrum, such as an edge or absorption line)⁵. These latter components just adjust the model by a factor depending on the energy⁵. Convolution and mixing models can then perform sophisticated operations on the result⁷¹. These include processes such as smoothing (e.g. velocity broadening), Compton reflection and detector pileup. If multiple spectra are analyzed simultaneously "mixing" models that link spectra are useful⁵. Models are defined in algebraic notation. So, for instance:

$$M1 * M2 * (A1 + A2 + M3 * A3) + A4$$

where M_i are multiplicative components and A_i are additive.

As any spectra fitting software, Sherpa comes with an extensive suite of models to fit the spectra, however, it also implements models from XSPEC. The three XSPEC models used for the spectral fitting in this work are explained below.

- `xsgaussian`: A simple Gaussian line profile. If the width ≤ 0 then it is treated as a delta function.

$$A(\lambda) = \frac{K}{\sigma \sqrt{2\pi}} \exp\left[-\frac{(\lambda - \lambda_l)^2}{2\sigma^2}\right], \quad (2.18)$$

where the parameters:

- `par1`= λ_l : line wavelength in Angstrom
- `par2`= σ : line width in Angstrom
- `norm`= K : total photons/cm²/s in the line

- **xsapc**: It models an emission spectrum from collisionally-ionized diffuse gas calculated from AtomDB atomic database**. More information can be found at it. For this model the parameters are:
 - **par1**: plasma temperature, keV
 - **par2**: Metal abundances (He fixed at cosmic). The elements included are C, N, O, Ne, Al, Si, S, Ar, Fe, Ni. The default relative abundance is set to 1.0
 - **par3**: Redshift, z
 - **norm**: $\frac{10^{-14}}{4\pi[D_A(1+z)]^2} \int n_e n_H dV$, where D_A is the angular diameter distance to the source (cm), n_e and n_H are the electron and H densities (cm^{-3}), respectively.
- **xspowlaw**: It is a simple photon power-law.

$$A(E) = KE^{-\alpha}. \quad (2.19)$$

where:

- **par1**= α : photon index of the power-law (dimensionless)
- **norm**= K : photons/keV/s at 1 keV

Fit and Confidence Intervals

The primary task of Sherpa is to fit a model $M(p_1, p_2, \dots)$ to a set of observed data, with p_i the model parameters⁶. An *optimization method* is one that is used to determine the parameters values for which the fit statistic, i.e. χ^2 , is minimized. Optimization has no guarantee that, for a given model and dataset, there will not be multiple local minimum of the statistics. Sherpa provides then different optimization methods and the default one, used in this work, is The Levenberg-Marquadt optimization method⁶⁸. The method finds the local minimum of nonlinear least squares functions of several variables by a modification of the Levenberg-Marquardt algorithm⁷². The algorithm relies on the software calculating the second derivative of the fit statistic with respect to the model parameters. By default, the calculation is analytic, assuming that the second derivatives of the model may be ignored⁶.

At the end of the fit, Sherpa writes out the best-fit parameter values and estimated confidence intervals. These confidence intervals are from the second derivatives of the fit statistic with respect to the model parameter values at the best-fit. They should be used for indicative purposes only as they are not reliable⁷¹.

2.6 Lightcurves

Lightcurves are practical on timing analysis. There are no calibration files specifically used for such purposes. Therefore, it is a simple histogram constructed with the counts on the event file and the TIME column on the file. However, a few issues should be considered when building lightcurves, e.g. dithering effects could move the source

**<http://www.atomdb.org>

in and out of the detector, bright sources may require time corrections to account recovery times between registering counts and being able to detect new events or the detector may experience telemetry saturation thus underestimating the event counts. Such issues are usually detected and thus observation specific documentations should be checked⁵.

Timing analysis with lightcurves is very important on X-ray astronomy since it can show attributes like background flares, periodic signatures and so on.

Chapter 3

Results & Discussion

3.1 Methodology

To track and see patterns of variation of past activity of Sgr A* it was used a selection on the available data from observations of Sgr A* from 2001 to 2017. The selection of the observations from 2001 to 2011 is identical to the one made by Clavel *et al.*⁶⁴ in their study on "*Echoes of multiple outbursts of Sagittarius A* released by Chandra*". The selection of data retrieved from 2012 to 2017 was made based on having large exposure times in order to perform better analysis. All data retrieved is detailed on tables 3.1 & 3.2. Most of the selected observations were pointed towards Sgr A* but due to different observations strategies or different CCDs used on the ACIS instrument, some regions are not uniformly covered.

The work described in this section follows the analysis made on Clavel *et al.*⁶⁴ and adapts their procedure. The data used was the latest available data from the archive as of January 2019 which includes up-to-date astrometry and energy calibration. The data reduction and analysis was performed using Chandra software at its latest version, 4.11.

The first thing to do after retrieving all the observations to be analyzed is to apply the latest calibration to all the data products. This is done directly via the command line with the command: `chandra_repro indir outdir`; where `indir` is the directory of each observation and `outdir` was left to the default value, i.e. the same directory as `indir`. This routine applies the automated data processing generating new data product files, i.e. new bad pixel file, new event file, new PHA file among others.

After applying the latest calibration, lightcurves are constructed on each observation to detect and reject times of background flares on the observation; this has the following procedure: first identify and filter any point source from the FOV, extract the background lightcurve to detect any flare period and finally cut such time intervals from the event file. This process was applied to all the observations per year at a time.

N	Date	Time (ks)	Obs. ID	Pointing (l,b)	Instrument
1	2001 Jul 18	11.5	2273	(0.195,-0.195)	ACIS-I
2	2001 Jul 18	11.3	2276	(0.195,0.000)	ACIS-I
3	2001 Jul 18	10.5	2282	(0.000,-0.195)	ACIS-I
4	2001 Jul 18	10.5	2284	(360.000,0.000)	ACIS-I
5	2002 Feb 19	12.4	2951	Sgr A*	ACIS-I
6	2002 Mar 23	11.4	2952	Sgr A*	ACIS-I
7	2002 Apr 19	10.2	2953	Sgr A*	ACIS-I
8	2002 May 07	12.0	2954	Sgr A*	ACIS-I
9	2002 May 22	29.7	2943	Sgr A*	ACIS-I
10	2002 May 24	33.9	3663	Sgr A*	ACIS-I
11	2002 May 25	160.7	3392	Sgr A*	ACIS-I
12	2002 May 28	156.6	3393	Sgr A*	ACIS-I
13	2002 Jun 03	89.3	3665	Sgr A*	ACIS-I
14	2003 Jun 19	24.7	3549	Sgr A*	ACIS-I
15	2004 Jun 09	97.0	4500	(0.122,0.019)	ACIS-I
16	2004 Jul 05	49.3	4683	Sgr A*	ACIS-I
17	2004 Jul 06	49.0	4684	Sgr A*	ACIS-I
18	2004 Aug 28	5.1	5360	Sgr A*	ACIS-I
19	2005 Jul 24	48.3	5950	Sgr A*	ACIS-I
20	2005 Jul 27	44.6	5951	Sgr A*	ACIS-I
21	2005 Jul 29	44.3	5952	Sgr A*	ACIS-I
22	2005 Jul 30	35.9	5953	Sgr A*	ACIS-I
23	2005 Aug 01	16.7	5954	Sgr A*	ACIS-I
24	2005 Feb 27	4.6	6113	Sgr A*	ACIS-I
25	2006 Apr 11	2.5	6639	Sgr A*	ACIS-I
26	2006 May 03	4.8	6640	Sgr A*	ACIS-I
27	2006 Jun 01	4.9	6641	Sgr A*	ACIS-I
28	2006 Jul 04	5.0	6642	Sgr A*	ACIS-I
29	2006 Jul 17	29.3	6363	Sgr A*	ACIS-I
30	2006 Jul 30	4.9	6643	Sgr A*	ACIS-I
31	2006 Aug 22	4.6	6644	Sgr A*	ACIS-I
32	2006 Sep 25	4.2	6645	Sgr A*	ACIS-I
33	2006 Oct 29	4.3	6646	Sgr A*	ACIS-I
34	2007 Feb 14	38.0	7048	(0.184,-0.199)	ACIS-I
35	2007 Feb 11	4.8	7554	Sgr A*	ACIS-I
36	2007 Mar 25	4.9	7555	Sgr A*	ACIS-I
37	2007 May 17	4.8	7556	Sgr A*	ACIS-I
38	2007 Jul 20	4.7	7557	Sgr A*	ACIS-I
39	2007 Sep 02	4.7	7558	Sgr A*	ACIS-I
40	2007 Oct 26	4.9	7559	Sgr A*	ACIS-I

Table 3.1: Chronological ordered list of downloaded and analyzed observations, part I. The table shows observation date, observation time, observation ID, main pointing in galactic coordinates (Sgr A* is at (l,b)=(359.944°, -0.046°)) and ACIS type instrument.

N	Date	Time (ks)	Obs. ID	Pointing (l,b)	Instrument
41	2008 May 05	27.5	9169	Sgr A*	ACIS-I
42	2008 May 06	26.4	9170	Sgr A*	ACIS-I
43	2008 May 10	27.5	9171	Sgr A*	ACIS-I
44	2008 May 11	27.3	9172	Sgr A*	ACIS-I
45	2008 Jul 25	27.5	9174	Sgr A*	ACIS-I
46	2008 Jul 26	27.4	9173	Sgr A*	ACIS-I
47	2009 May 18	110.6	10556	Sgr A*	ACIS-I
48	2010 May 13	78.5	11843	Sgr A*	ACIS-I
49	2011 Jul 19	30.6	13508	(0.013,-0.088)	ACIS-I
50	2011 Jul 21	56.1	12949	(0.013,-0.088)	ACIS-I
51	2011 Jul 29	64.8	13438	(0.013,-0.088)	ACIS-I
52	2012 Jul 24	173.9	13839	Sgr A*	ACIS-S
53	2012 Jul 26	160.4	13840	Sgr A*	ACIS-S
54	2012 Jul 17	44.5	13841	Sgr A*	ACIS-S
55	2012 Aug 01	98.3	13838	Sgr A*	ACIS-S
56	2013 Jul 27	45.4	15041	Sgr A*	ACIS-S
57	2013 Aug 11	45.7	15042	Sgr A*	ACIS-S
58	2013 Sep 14	45.4	15043	Sgr A*	ACIS-S
56	2013 Oct 04	42.7	15044	Sgr A*	ACIS-S
57	2014 Mar 14	41.8	16211	Sgr A*	ACIS-S
58	2014 Apr 04	45.4	16212	Sgr A*	ACIS-S
59	2014 Apr 28	45.0	16213	Sgr A*	ACIS-S
60	2014 May 20	45.4	16214	Sgr A*	ACIS-S
61	2015 Apr 25	79.0	17236	Sgr A Complex 1	ACIS-I
62	2015 May 14	22.7	16966	Sgr A*	ACIS-S
63	2015 Aug 17	22.7	16965	Sgr A*	ACIS-S
64	2015 Oct 21	22.6	16964	Sgr A*	ACIS-S
65	2016 May 18	52.4	18852	Sgr A*	ACIS-I
66	2016 Jul 12	78.4	18731	Sgr A*	ACIS-S
67	2016 Jul 18	76.6	18732	Sgr A*	ACIS-S
68	2016 Oct 14	22.7	18058	Sgr A*	ACIS-S
69	2017 Jul 15	81.0	19703	Sgr A*	ACIS-S
70	2017 Jul 25	78.4	19704	Sgr A*	ACIS-S
71	2014 Apr 06	28.8	19726	Sgr A*	ACIS-S
72	2014 Apr 07	27.8	19727	Sgr A*	ACIS-S

Table 3.2: Chronological ordered list of downloaded and analyzed observations, part II. The table shows observation date, observation time, observation ID, main pointing in galactic coordinates (Sgr A* is at (l,b)=(359.944°, -0.046°)) and ACIS type instrument.

First though, it is important to note that prior applying any routine it is important to check that the correct bad pixel file is selected for each observation. This is done by manually choosing the correct file and assigning it to the `ardlib` routine with the command `acis_set_ardlib xxxx_bpix1.fits`. Another important cautionary measure before applying any routine is to "punlearn" the tool, i.e. restore the system default parameters of the tools. So, `punlearn ardlib` restores all the values of the `ardlib` routine. This is important to avoid errors due to wrong parameters from other implementation stored on the parameter files of the tools.

Said that, to identify point sources on the observation the CIAO routine `celldetect` was applied. It searches point sources by summing counts in square cells ("detect" cells) in the dataset and comparing the counts to those of "background" cells⁶⁶. This tool was applied on square cells of 9 pixels, thus the cell size is not allowed to vary. `celldetect` creates regions enclosing the point sources and creates a region file which can be used to filter the event file. The routine used to create such region files is:

```
for obsid in {19703,19704,19726,19727}; do
cd $obsid/repro/;
punlearn ardlib;
acis_set_ardlib acisf${obsid}_repro_bpix1.fits;
punlearn celldetect;
pset celldetect infile=acisf${obsid}_repro_evt2.fits;
pset celldetect outfile=acisf${obsid}_src.fits;
pset celldetect regfile=acisf${obsid}_src.reg;
pset celldetect fixedcell=9; celldetect;
cd .. && cd ..;
done$
```

This is an explicit example of the implementation over the observations of the year 2017. To visualize an example of the point source detection with `celldetect` on an observation processing, see Appendix B.

Once this is done, it is possible to extract the background lightcurves. The `dmextract` routine crates an histogram of counts and a column from a table file, i.e. the event file. When selected the TIME column it constructs the lightcurve with a simple linear binning⁶⁶. First, from the event file it was filtered out the energy ranges outside 0.3 to 7 keV because in this region the ACIS background is fairly flat⁶⁶. This is done with the `dmcopy` tool. From this filtered file the lightcurve was extracted. Thereafter, the `deflare` routine was used to filter the flares from the lightcurve. It performs an iterative algorithm that removes the counts falling outside a given interval ($\bar{x} - n\sigma, \bar{x} + n\sigma$). `deflare` creates a GTI filter which can be used to filter out, with `dmcopy`, the flare time intervals. This procedure was done twice, with the interval ($\bar{x} - 2\sigma, \bar{x} + 2\sigma$). Thus, the extraction of the lightcurve and the latter removal of the flares was as follows:

```
for obsid in {19703,19704,19726,19727}; do
cd $obsid/repro/;
punlearn ardlib;
```

```

acis_set_ardlib acisf${obsid}_repro_bpix1.fits;
punlearn dmextract;
dmcop "acisf${obsid}_repro_evt2.fits[energy=300:7000]" acisf${obsid}_efilt.fits;
pset dmextract "acisf${obsid}_efilt.fits[exclude sky=region(acisf${obsid}_src.reg)]
    [bin time>::200]";
pset dmextract outfile=lc_acisf${obsid}.fits;
pset dmextract opt=ltc1;
dmextract;
deflare lc_acisf${obsid}.fits outfile=${obsid}.gti method="sigma" nsigma=2 plot=yes;
dmcop "acisf${obsid}_efilt.fits[@${obsid}.gti]" acisf${obsid}_def_1.fits;
punlearn dmextract;
pset dmextract "acisf${obsid}_def_1.fits[exclude sky=region(acisf${obsid}_src.reg)]
    [bin time>::200]";
pset dmextract outfile=lc_acisf${obsid}_2.fits;
pset dmextract opt=ltc1;
dmextract;
deflare lc_acisf${obsid}_2.fits outfile=${obsid}_2.gti method="sigma" nsigma=2 plot=yes;
dmcop "acisf${obsid}_def_1.fits[@${obsid}_2.gti]" acisf${obsid}_def_2.fits;
cd .. && cd ..;done

```

Again, it is an explicit example performed on the observations of the year 2017. There it can be seen the parameter `opt=ltc1` for `dmextract`, it tells `dmextract` to make the histogram with the `TIME` column. It can be seen also that the binning was into 200 second time bins. To visualize an example of an observation-specific lightcurve and its flare cleaning, see Appendix B.

To estimate the background contribution, CIAO provides blank sky event files. Such files can be retrieved and automatically be matched to the astrometry of the event file with the `blansky` command which works with the auxiliary `asol.fits` file in the data products (see Appendix A). The `blansky` background file produced for each observation can later be used on both imaging and spectral analysis. The following was applied to obtain them.

```

for obsid in {19703,19704,19726,19727}; do
cd $obsid/repro/;
punlearn ardlib;
acis_set_ardlib acisf${obsid}_repro_bpix1.fits;
punlearn blansky;
pset blansky evtfile="acisf${obsid}_repro_evt2.fits[@${obsid}.gti][@${obsid}_2.gti]";
pset blansky outfile=${obsid}_blank.evt;
pset blansky tmpdir=./;
blansky mode=h;
cd .. && cd ..; done

```

It is important to note that the input event file for `blanksky` must not be filtered in energy, so that the original event file is used applying the GTI filters from `deflare`. By estimating the background with this `blanksky` files, instrumental lines and Galactic low-energy emission are not traced⁶⁴. Again, this was the explicit implementation on observations of year 2017.

At this point, the data was processed enough to perform the analysis specific routines. The steps performed to obtain flux mosaics and fitted spectra are as follows:

- **Central Region Flux Mosaics:** To build flux mosaics it is first needed to build exposure maps and exposure corrected images for each observation and then reproject and combine them on a single exposure corrected mosaic. This process is automated by the `merge_obs` routine on CIAO; it creates exposure maps and images for each observation and then reprojects them to a common tangent point. When calling `merge_obs`, a particular energy band can be chosen and therefore look up to the flux mosaic correspondent to a particular emission, i.e. Fe $K\alpha$ line. Flux mosaics on the broad band, i.e. 0.5-7.0 keV, were built for three periods: 2001-2006, 2007-2011 and 2012-2017. Every observation from each year was used to construct the respective flux mosaic. An example of such implementation, in this case of the period 2001-2006, is:

```
merge_obs "*/repro/*def_2*" Sgr_A_first/ bands=broad
```

where all the observations corresponding this period were on the same directory for easy instruction on the command line. There is also the possibility of doing this process manually by first constructing the flux and exposure maps for each observation with the `fluximage` routine and then combine the images and exposure maps with the `reproject_image` routine.

After building the three flux mosaics, they can be put together on an RGB map to visualize the variation of the emission across the years. To construct such map, the three mosaics are imported to the GUI of DS9, see Joye and Mandel⁶⁷.

- **Sgr A* Spectrum:** To constrain the Fe $K\alpha$ line variability, the spectral shape of the emission was studied by fitting it with a simple model. To obtain good statistics, the analysis was performed on the years: 2002, 2004, 2006, 2008, 2010, 2011, 2012, 2014, 2016 and 2017.

In each observation the `specextract` routine was applied to extract source and background spectra for extended regions and build the associated response files, ARF and RMF. This routine extracts spectra from ACIS-I data and can also be applied on ACIS-S data, but only taking account zeroth-order grating data. After this, the `combine_spectra` routine was applied to improve the counts, combining the spectra of each year. It combines the PHA file and the associated response files. This procedure slightly increases the width of the Fe $K\alpha$ line as the energy calibration on each observation varies⁶⁴, so this parameter should not be confidently used during analysis. The implementation of the routines is as follows:

```
for obsid in {19703,19704,19726,19727}; do
cp src.reg ${obsid}/repro/;
cp bkg.reg ${obsid}/repro/;
```



```

cd $obsid/repro/;
punlearn ardlb;
acis_set_ardlib acisf${obsid}_repro_bpix1.fits;
punlearn specextract;
pset specextract infile="acisf${obsid}_def_2.fits[sky=region(src.reg)]";
pset specextract outroot=${obsid}_2_spec;
pset specextract bkgfile="${obsid}_blank.evt[sky=region(bkg.reg)]";
pset specextract bkgresp=no;
specextract;
cd .. && cd ..;
done
combine_spectra /${obsid}/repro/*spec.pi 2017_spec

```

In the `bkgfile` it can be seen the application of the `blanksky` file and the regions of source and background from where the spectra are being extracted are defined by the `.reg` files. The parameter `bkgresp=no` means that the routine does not create response files for the background spectra, this is a restriction of the routine when using `blanksky` files. Once more, the example was the actual implementation of the routines on 2017 observations

Once the spectra are extracted and combined, it is ready to be loaded on Sherpa and fitted. The spectra of the years 2002, 2004, 2006, 2008, 2010, 2011, 2012, 2014, 2016 and 2017 was loaded simultaneously an Sherpa to do the fit also simultaneously. To improve the performance of the spectral fit, spectrum counts were grouped with the `group_counts` routine inside Sherpa which combines the data so that each bin contains at least a specific number of counts. It was applied to have at least forty counts per bin.

The spectral energy range was restricted to 4-7.1 keV because the reflection contribution is larger and soft plasma contribution is reduced⁶⁴. Previous studies^{64 65 73 74} have demonstrated the compatibility of the spectrum with a superposition of a reflection spectrum and a thermal component. Then, the spectrum is fitted by a model consisting of a Gaussian Fe $K\alpha$ emission line added to a photon power-law and a thermal emission characterized by a 6.5 keV temperature plasma^{64 9}. This is done implementing the Xspec model: `xsgaussian + xspowerlaw + xsapex` to fit the data inside Sherpa. The hot-plasma component is expected to be constant across the years while the reflection of high-energy emission induces the Fe $K\alpha$ line to vary in a correlated way⁶⁴.

To reduce the number of free parameters of the fit, the plasma temperature was fixed to 6.5 keV and the normalization was set to be the same across all the years. Therefore, a total of $10 \times 5 + 1$ free parameters were fitted simultaneously. The free parameters were: the hot-plasma normalization, the ten years iron line width, position and amplitudes and the ten years photon indices and normalization.

The implementation of this process in Sherpa is as follows:

```
load_pha(id, "name.pi")
```

```

set_analysis('energy')
ignore(":4,7.1:")
group_counts(id,40)
subtract(id) # to subtract background spectrum
set_source(id, xsgaussian.gausid + xspowerlaw.powid + xsapex.apecid)
apecid.kT = 6.5 # for all years, fixing plasma temperature
freeze(apecid.kT) # for all years
guess(apecid) # from second year and after
apecid.norm = apec1.norm # linking to be the same all years, from second year and after
fit()
plot_fit_delchi()

```

where `id` stands for the identification given to each year spectrum and `name.pi` is a generic name for the spectrum file. Sherpa reads automatically the auxiliary response files and background.

3.2 Flux Mosaics of the Central Region

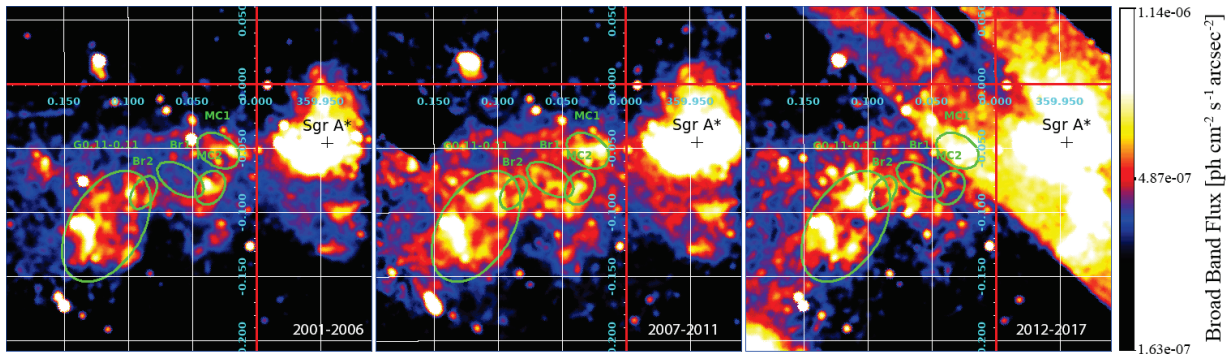


Figure 3.1: *Left*: Broad band flux mosaic map on the years 2001-2006. *Middle*: Broad band flux mosaic map on the years 2007-2011. *Right*: Broad band flux mosaic map on the years 2012-2017. These images are smoothed to 4 arcsec. The three images are on the same logarithmic scale and color bar settings. This shows an apparent increasing trend on the broad band X-ray emission. The coordinate grid displayed is in galactic coordinates. The molecular structures, i.e. labeled regions, are based and estimated from the flux maps presented on Ponti *et al.*⁶⁵ and Clavel *et al.*⁶⁴.

The flux mosaics corresponding to the periods 2001-2006, 2007-2011 and 2012-2017 are on figure 3.1. In these maps it can be recognized similar molecular cloud structures as in flux mosaics presented in Clavel *et al.*⁶⁴ and Ponti *et al.*⁶⁵; therefore, the regions have been labeled in a similar way. Those works presented a study on the past activity of Sgr A* and concluded that past flares coming from Sgr A* might be the origin of the variability seen

on the molecular clouds emission. Particularly, Clavel *et al.*⁶⁴ characterized the emission variability of the bridge region to have a 2-year peaked variation. Such variation could be related with short time flares from a quick increase of Sgr A^{*} activity. The mosaics show the illumination distribution of the X-ray emission from the molecular clouds. Particularly, it can be seen a slight increase on the emission from the first period to the second one followed by a little decrease up to the third period.

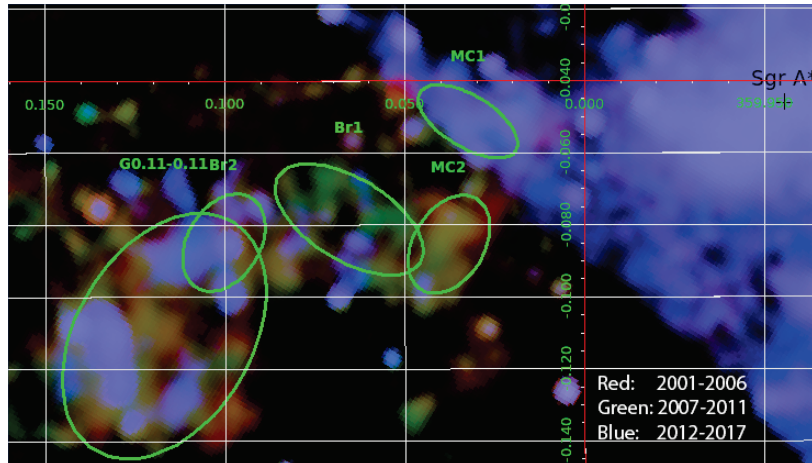


Figure 3.2: RGB mosaic map smoothed to 4 arcsec. In red is the contribution from years 2001-2006. In green, contribution corresponding to 2007-2011 and in blue for the years 2012-2017. Note that the scales are slightly different from blue, green and red colors; this was done to better visualize the colors on the map. The coordinate grid displayed is in galactic coordinates. The molecular structures described on Clavel *et al.*⁶⁴ and Ponti *et al.*⁶⁵ are also recognizable. Again, it is apparent the increase in activity as the RGB map appears blueish overall. In the MC2 region, the emission has varied in a trend from west to east, similar to what it is shown in Clavel *et al.*⁶⁴. Also similar, the Br1 & Br2 regions show a late illumination and the G0.11-0.11 cloud having complex variations. MC1 region is placed on a zone of the RGB map showing rare artifacts.

The fact that the flux images in Fig. 3.1 show an overall increasing emission tendency could mean further short period variations, such as the ones described on Clavel *et al.*⁶⁴, on the bright regions as well as a rather extended variation on scale of decades. However, the fact that most of the data used for the last flux image (2012 to 2017 period) is coming from spectroscopic observations, i.e. ACIS-S detector, rather than imaging, prevents from doing such affirmations. Instead, it can only be argued that the short time scale variation concluded on Clavel *et al.*⁶⁴ is confirmed not only from the emission characterizing the neutral Fe K α line but also in the broad band emission shown in these mosaics.

Also, it is evident the presence of quite rare artifacts on the image (for instance, the bright section on the bottom left corner of the last flux image or even worse, the regions near Sgr A^{*} on the same image). It may be regarded to a bad processing of background or not enough background statistics on the data corresponding to the 2012-2017 period given that most of it is from ACIS-S detector.

The RGB map shown in figure 3.2 is a pretty useful map also. Further than making apparent an increase in emission, it also illustrates a directional trend in the variation of the emission. For instance, the MC2 region shows a trend of the emission increase from right to left, i.e. from west to east. MC1 cloud is situated on a region exhibiting background artifacts so that nothing can be inferred about the variation patterns on it. Br1 region has a greater illumination on the second period, in agreement with what the RGB map in Clavel *et al.*⁶⁴ shows, and Br2 has a late illumination on the last period mainly. G0.11-0.11 region has a complex illumination variation patterns, again in agreement with what is shown in Clavel *et al.*⁶⁴.

3.3 Spectral Analysis

The fitted spectra generated for the years 2002, 2004, 2006, 2008, 2010, 2011, 2012, 2014, 2016 and 2017 are shown in the figures 3.3, 3.4, 3.5, 3.6. The error bars are given by the confidence interval of the fit, 1σ . The fit results are shown in table 3.3. The spectra were extracted by imaging spectroscopy from the bright region in the vicinity of Sgr A*, i.e. the region containing a dense and luminous star cluster as well as several components of neutral, ionized and extremely hot gas¹².

Parameters	2002	2004	2006	2008	2010
Fe K α Norm (10^{-4} ph cm $^{-2}$ s $^{-1}$)	1.7 ± 0.08	2.8 ± 0.1	2.3 ± 0.1	1.9 ± 0.1	1.7 ± 0.1
Continuum Photon Index	1.45 ± 0.08	1.36 ± 0.08	1.18 ± 0.09	0.47 ± 0.05	1.34 ± 0.12
Continuum Norm (10^{-3} ph keV $^{-1}$ cm $^{-2}$ s $^{-1}$)	2.7 ± 0.4	2.8 ± 0.4	2.3 ± 0.4	1.2 ± 0.1	2.3 ± 0.4
Degrees of freedom, ν	199	200	199	201	193
Statistic, χ^2	196.634	187.713	157.65	235.753	132.651
Reduced statistic, χ^2/ν	0.988	0.939	0.792	1.173	0.687
	2011	2012	2014	2016	2017
Fe K α Norm (10^{-4} ph cm $^{-2}$ s $^{-1}$)	2.3 ± 0.09	2.4 ± 0.06	0.2 ± 0.04	0.8 ± 0.08	0.6 ± 0.06
Continuum Photon Index	1.48 ± 0.08	1.13 ± 0.05	1.64 ± 0.06	0.88 ± 0.03	1.03 ± 0.1
Continuum Norm (10^{-3} ph keV $^{-1}$ cm $^{-2}$ s $^{-1}$)	3.1 ± 0.4	2.2 ± 0.2	4.0 ± 0.4	3.3 ± 0.2	0.8 ± 0.1
Degrees of freedom, ν	200	201	200	201	200
Statistic, χ^2	193.981	397.864	183.237	263.513	214.366
Reduced statistic, χ^2/ν	0.97	1.98	0.916	1.311	1.07

Table 3.3: Best fit parameters for the nine year simultaneous fit obtaining a total reduced statistic of $\chi^2/\nu = 2163.36/1994 = 1.08$. Again, the continuum emission is modeled by a simple power-law with a not straightforward interpretation. The obtained hot plasma normalization was $(4.56 \pm 0.49) \times 10^{-3} \text{cm}^{-5}$. The other parameters were fixed as explained before in section 3.1.

The overall reduced statistic $\chi^2/\nu = 1.08$ shows an optimum fit on the simultaneously fitted spectra. The obtained spectra show the Fe K α emission variability; recall that this line is attributed from fluorescence from photoionized matter in the vicinity of the compact, bright source⁷⁵, i.e. Sgr A*. Specifically, Sunyaev *et al.*³¹ and Koyama

*et al.*⁹ suggested that the Fe $K\alpha$ line may be produced in molecular clouds, along with a non-thermal radiation X-ray continuum radiation, as a result of reprocessed emission of powerful X-ray flares coming from the SMBH Sgr A*¹⁰. However, other mechanisms have been suggested to produce the emission line; e.g. from cosmic rays interaction with the molecular clouds⁶⁵, large populations of accelerated electrons in the galactic center^{76,57} or sub-relativistic protons generated by star accretion partly exciting and generating the emission line^{77,78}.

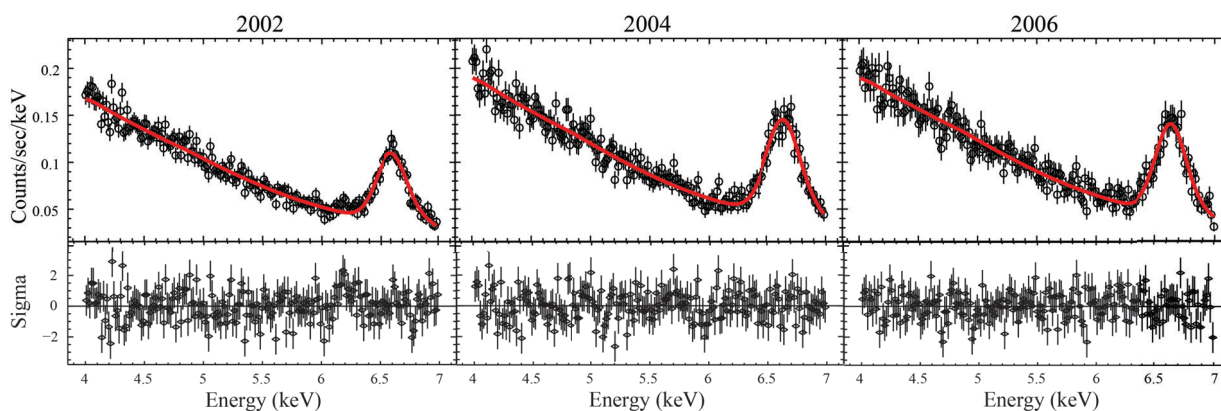


Figure 3.3: Emission spectra from the years 2002,2004 and 2006. The spectra was extracted from the bright region on top of the cross mark Sgr A* in 3.1 and 3.2. A slight increase in the Fe $K\alpha$ peak is appreciable.

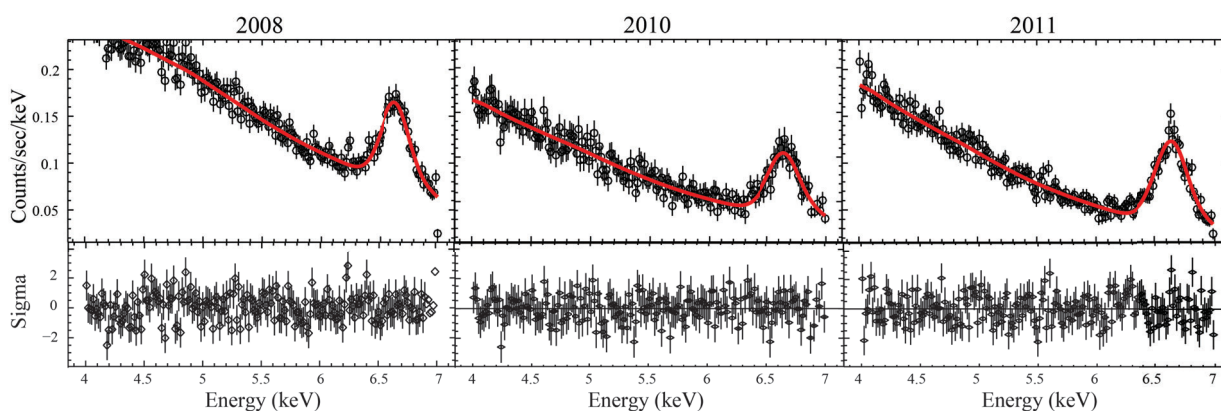


Figure 3.4: Emission spectra from the years 2008, 2010 and 2011. The spectra was extracted from the bright region on top of the cross mark Sgr A* in 3.1 and 3.2. Previous noted increase kept constant for various years.

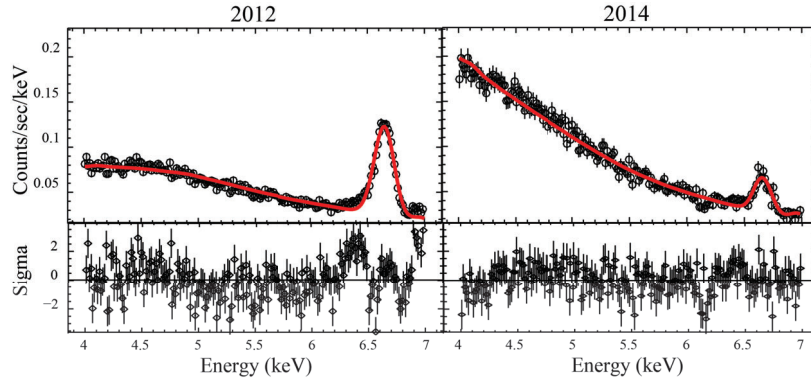


Figure 3.5: Emission spectra from the years 2012 and 2014. The spectra was extracted from the bright region on top of the cross mark Sgr A^{*} in 3.1 and 3.2. There is an abrupt decrease on the background emission around the Fe K α line on the 2012 spectrum which increases after while the Fe K α line decreased its peak on 2014.

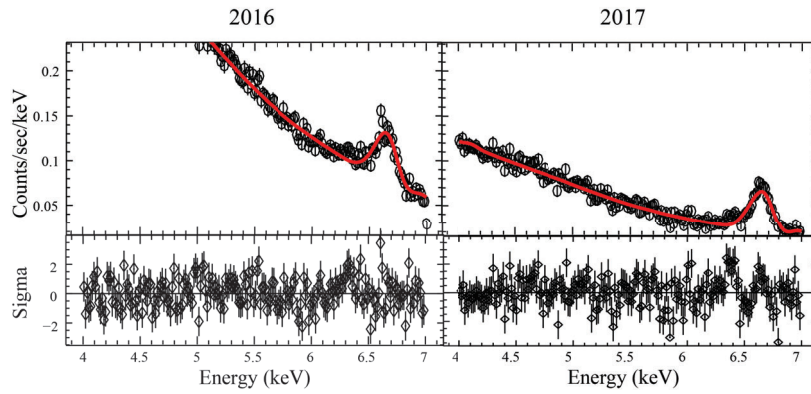


Figure 3.6: Emission spectra from the years 2016 and 2017. The spectra was extracted from the bright region on top of the cross mark Sgr A^{*} in 3.1 and 3.2. It is shown a abrupt change on the spectrum comparing with the other spectra. It may be attributed to a flare period not filtered on the deflaring steps. The last spectrum follows the trend shown in the spectra from 2012 and 2014.

Looking at the spectra, it appears a slight increase of the Fe K α line peak from 2002 to 2004 ($1.7 \rightarrow 2.8 \times 10^{-4} \text{ ph cm}^{-2} \text{ s}^{-1}$) and then a following decreasing trend up to 2010 ($2.8 \rightarrow 2.3 \rightarrow 1.9 \rightarrow 1.7 \times 10^{-4} \text{ ph cm}^{-2} \text{ s}^{-1}$). Thereafter, an increasing trend shows up again up to 2012 ($1.7 \rightarrow 2.3 \rightarrow 2.4 \times 10^{-4} \text{ ph cm}^{-2} \text{ s}^{-1}$) followed by an abrupt decrease on 2014 ($2.4 \rightarrow 0.2 \times 10^{-4} \text{ ph cm}^{-2} \text{ s}^{-1}$) and a progressive increase up to 2017 ($0.2 \rightarrow 0.8 \rightarrow 0.6 \times 10^{-4} \text{ ph cm}^{-2} \text{ s}^{-1}$). The continuum emission variation presents the following variations: it is kept constant with slight variations in the 2002 to 2011 period followed with an abrupt decrease in 2012 increasing again rapidly up

to 2016 and finally decreasing in 2017. At first, this behavior is in agreement with the X-ray emission variability attributed to Sgr A* emission. The interpretation of the power-law parameters is not as straightforward as the interpretation for the Gaussian model for the $K\alpha$ line that shows a correlated variation with what is seen in the spectra in figures 3.3, 3.4, 3.5 and 3.6 and the values of the norm in table 3.3. The parameter values of the power-law do not vary the same as the apparent variation from the spectra.

What is interesting to see is an apparent delay on the abrupt decrease that both continuum power-law and Fe $K\alpha$ Gaussian line experience in 2012 and 2014 respectively. One may wonder what this could mean physically, and in the interpretation of the Fe $K\alpha$ line as a reprocessed emission from past flares of the SMBH the following scenario is proposed that may explain this delay. As the continuum power-law can be regarded as the emission coming directly from Sgr A* without any reflection or reprocessing, it is possible that the activity of Sgr A* decreased thus generating the spectrum with a lower emission in the continuum power-law in the year 2012. The same emission is reprocessed by the molecular clouds in the vicinity of the SMBH producing the Fe $K\alpha$ line and, as the emission was decreased, generating a spectrum with an Fe $K\alpha$ line with a lower peak. However, as the X-ray emission takes longer time to be reflected in the molecular clouds near Sgr A* and then emitted towards the satellite, the continuum power-law and the Fe $K\alpha$ corresponding to the period of lower emission will reach the satellite detectors at different times so that the lower peak Fe $K\alpha$ line showed in the 2014 spectrum would correspond to the decreased emission seen in the 2012 spectrum continuum power-law. With this said, it is also important to note that it has been assumed that the continuum power-law is also affected by Sgr A* emission variability while it could be an inherent emission of the molecular clouds alone. Nevertheless, the Fe $K\alpha$ line variability indeed reflects the flaring variability nature of Sgr A*. Regarding the 2016 spectrum, the continuum power-law shows an increased emission. Following the same criteria as before, it is expected to have a delayed increase in the Fe $K\alpha$ peak. However, 2018 X-ray data was not available and, expecting the same time delay, this increase should appear on a 2018 Fe $K\alpha$ line.

In general, the spectra in figures 3.3, 3.4, 3.5 and 3.6 and also the parameter values in table 3.3 show cyclic variations of increasing and decreasing emission reflected on the increasing and decreasing nature of the Fe $K\alpha$ line peak. These results agree with the variable X-ray emission characteristic to the SMBH well described by studies on the Galactic Center. However, these results are not enough to ensure a characteristic strong flare on the analyzed data. Particularly, a period of reduced overall emission from Sgr A* could be inferred.

Chapter 4

Conclusions & Outlook

Along this work it has been introduced the basics on X-ray astronomy with a particular focus on the spectral characterization of the emission on the energy band containing the Fe $K\alpha$ line, an important emission characteristic of high energy phenomena and in particular of the galactic center emission. The visualization of the emission is equally important when analyzing emission variability, this is addressed by building flux maps; an introduction to building such maps was also reviewed along with important considerations and filtering of the raw data downloaded from the archives.

Specifically, it was performed an analysis of the emission variability coming from the compact radio source Sgr A*, the closest SMBH situated at the center of our galaxy, and its vicinities. The analysis was performed in data correspondent to the period spanning 2001 to 2017, the data was retrieved from Chandra's public archive and accessed with CIAO. After filtering background flaring periods and approximating the background with blank files provided in CIAO, in order to characterize the emission variability, flux mosaics correspondent to three periods (2001 to 2006, 2007 to 2011 and 2012 to 2017) with their correspondent RGB map and spectra of specific year samples (2002, 2004, 2006, 2008, 2010, 2011, 2012, 2014, 2016 and 2017) were constructed.

The flux mosaics allowed to visualize the emission variability in the broad band, i.e. 0.5 - 7.0 keV. The three different periods showed a different emission pattern with an overall increasing trend, i.e. even though the illumination patterns are brighter on the second period, the third period appears to be brighter than the first one. It is important to note that molecular clouds structures, similar to the ones described on Clavel *et al.*⁶⁴ and Ponti *et al.*⁶⁵ can be recognized on the constructed flux mosaics.

The RGB map build up from the flux mosaics of the three different periods allows to visualize not only individual illumination and structures but also it helps to visualize illumination variability (with directional trend) inside the recognized molecular clouds. Particularly, the MC2 cloud shows an illumination shifting from east to west, Br1 and Br2 structures show a late illumination corresponding the second and third period respectively and the G0.11-0.11 show a more complex illumination variability, MC1 cloud is inside a region showing rare artifacts and then a illumination variability cannot be seen. These results also coincide to results presented on Clavel *et al.*⁶⁴.

The spectral analysis helped to see the variability of the Fe $K\alpha$ emission. The spectra were fitted with a

simple model consisting of a thermal emission component, a photon power-law and a Gaussian profile emission line obtaining an overall good fit. In general, a cyclic variability of increasing and decreasing emission tendency was found on the spectra from the mentioned regions. Of particular interest was the variability seen in the years 2011, 2012 and 2014 in which, first, there is a prominent decrease of the continuum power-law and then a prominent decrease appears in the Fe $K\alpha$ peak. It is interpreted as the same decrease in activity/emission coming from Sgr A* but the Fe $K\alpha$ shows a delay on the decreasing tendency as it is a reprocessed emission on the molecular clouds.

The results showed an overall agreement with the known high X-ray variability nature of Sgr A* extensively studied. However, they are not strong enough to state a strong past flare coming from Sgr A*.

Studying the X-ray emission variability in the galactic center can give hints on the past activity of the SMBH at the Galactic Center and it also helps to visualize and characterize molecular clouds structures on the central region. A spectral analysis specifically done over the regions of each molecular cloud can give hints on the cloud physical attributes and also can give further hints on the past flaring nature of Sgr A* emission. Additionally, during this work it was evident the need of more rigorous criteria on selecting the data to be analyzed. Specially, mixing ACIS-I and ACIS-S observations led to rare artifacts on the flux mosaics construction and spectral resolution from ACIS-S is lost as the spectrum was extracted with imaging spectroscopy routines which kept only zeroth-order beams coming from the grating spectrometer.

Appendix A

Introduction to Chandra Data Products

As explained before, when a Chandra observation is taken, the CXC applies the SDP pipeline on it and the results are stored on the Chandra archive. When it is retrieved, a series of files and directories are downloaded. The directories and files are described bellow. The information shown in this chapter is based on the CIAO⁶⁶ threads on CIAO's website*

A.1 ObsID Directory

It is the top level directory. It contains three files and two data directories (the examples correspond to the ObsID 9173, an ACIS-I observation):

```
$ pwd
/9173
$ ls
00README  axaff09173N002_VV001_vv2.pdf  oif.fits  primary  secondary
```

- **V & V report:** It is a PDF file containing a summary report of the verification and validation process. A process done by CXC scientists on all data products to ensure data quality and investigate any anomalies on the data.
- **Observation index file:** This file contains a summary of the data products of the observation. It contains a structured directory list with descriptive information about the observation.
- **README:** The ASCII README file includes information on how to cite Chandra data in publications, acknowledging CIAO usage, Chips, and Sherpa.

*http://cxc.harvard.edu/ciao/threads/intro_data/

A.2 Primary Directory

All data products enough for most analysis are contained in this directory.

```
$ pwd
/9173/primary
$ ls
acisf09173_000N002_bpix1.fits      acisf09173N002_full_img2.fits
acisf09173_000N002_fov1.fits      acisf09173N002_full_img2.jpg
acisf09173N002_cntr_img2.fits      orbitf333374701N001_eph1.fits
acisf09173N002_cntr_img2.jpg      pcadf333495506N002_asol1.fits
acisf09173N002_evt2.fits
[hrc_dtf1.fits]
[acis_plt2.jpg]
[acis pha2.fits]
```

- **Images:** Every data set includes two images: a full-field sky image (`full_img2.jpg`) and a high-resolution image of the center of the field (`cntr_img2.jpg`). No energy filter is applied to these images. FITS images are also created but only for imaging observations. The rest of the files on this directory are the products necessary for analysis.
- **Level 2 event file** (`evt2.fits`): This is the most important data product. Created from the level one event list by filtering on GTI and bad pixels, cosmic rays, or streak events. It contains the list of events suitable to use in analysis.
- **Source list** (`scr2.fits`): A list of source candidates on the observations. It is generated from a single run of `celldetect` and should not be used directly in analysis.
- **Bad pixels** (`bpix1.fits`): A list of pixels defined as bad. Any tool reading this file while exclude such pixels from calculations.
- **Sky field of view** (`fov1.fits`): The field of view file contains regions delimiting the edges of the instrument chips. It can be used to filter event files on specific chips.
- **Orbit ephemeris** (`orbit_eph1.fits`): Orbit ephemeris information for the observation.
- **Aspect solution** (`pcad_asol1.fits`): Aspect solution describing the orientation of the telescope as function of time. There may be more than one `asol1` files for an observation. The detected position and corresponding telescope aspect are combined to determine the event celestial position.
- **Dead time factor** (`dtf1.fits`): for HRC observations only. The file contains dead time correction factors as function of time. ACIS observations include this information on the event file.

- **Type II PHA/Spectra** (`pha2.fits`): Only for grating observations (HRC/LETG or ACIS/HETG). This file contains a spectrum for one grating part and order in each row of the file.

A.3 Secondary Directory

This data is useful when reprocessing the data. It contains level 1 files:

```
$ pwd
/9173/secondary
$ ls
acisf09173_000N002_evt1.fits      acisf333493891N003_3_bias0.fits
acisf09173_000N002_flt1.fits      acisf333493891N003_4_bias0.fits
acisf09173_000N002_msk1.fits      acisf333493891N003_5_bias0.fits
acisf09173_000N002_mt11.fits      acisf333495207N003_pbk0.fits
acisf09173_000N002_stat1.fits      aspect
acisf333493891N003_0_bias0.fits     axaff09173N002_VV001_vvref2.pdf
acisf333493891N003_1_bias0.fits     ephem
acisf333493891N003_2_bias0.fits
[acis_evt1a.fits -or- hrc_evt1a.fits]
[hrc_std_flt1.fits]
[hrc_std_dtfstat1.fits]
```

- **V & V report** (`vvref2.pdf`): full V & V report of the observation.
- **Aspect offsets** (`aoff1.fits`): Set of offsets versus time. Derived from the aspect solution files on primary directory.
- **Level 1 event file** (`evt1.fits`): It contains all the events recorded on the observation. Although many of these events may be characterized as bad, none of the information is filtered. This file is filtered to create the level 2 event file.
- **Level 1.5 event file** (`evt1a.fits`): Created for grating observations. It contains additional information related to the gratings, e.g. grating order, arm used (HEG or MEG), and wavelength.
- **Good time intervals** (`flt1.fits/std_flt1.fits`): Start and stop times of all accepted time intervals of the observations is stored on this file. Named slightly different for ACIS `flt1.fits` and HRC `std_flt1.fits` observations.
- **Mask** (`msk1.fits`): It contains the valid part of the detector elements used on the observation (ACIS CCDs or HRC plate). This is used to create response files.

- **Mission timeline** (`mtl1.fits`): The mission timeline consists of all time series that affects the quality of the data. Used to construct GTI limits on the good time intervals file.
- **Alignment offsets** (`soff1.fits`): Science instrument module versus time. It is derived from the aspect solution file in the primary directory.
- **Exposure statistics** (`stat1.fits`): Only for ACIS observations. Contains information on the sequence of ACIS CCD exposures processed and recorded into telemetry.
- **Dead time factor statistics** (`std_dtfstat1.fits`): Only for HRC observations. Dead time factor statistics information from the dead time factor file in the primary directory.
- **Bias maps** (`bias0.fits`): Only for ACIS observations To create the bad pixel file, each bias map is searched for pixels with bias values too high or too low.
- **Parameter block** (`pbk0.fits`): Only for ACIS observations. Used along the bias maps to create the bad pixel file. Contains observational parameters, e.g. active CCDs.
- **Aspect Subdirectory**: contains the `aqual1.fits` and aspect solution files based on aspect determined by the on-board computer (`osol1.fits`).

```
$ pwd
/9173/secondary/aspect
$ ls
pcadf333493899N002_osol1.fits  pcadf333511021N002_osol1.fits
pcadf333495506N002_aqual1.fits  pcadf333517581N002_osol1.fits
pcadf333497901N002_osol1.fits  pcadf333520631N002_osol1.fits
pcadf333504461N002_osol1.fits
```

- **Ephem Subdirectory** Contains solar (`solar_eph1.fits`), lunar (`lunar_eph1.fits`) ephemeris files and viewing angles file (`angles_eph1.fits`)

```
$ pwd
/9173/secondary/ephem
$ ls
anglesf09173_000N002_eph1.fits  solarf333374701N001_eph1.fits
lunarf333374701N001_eph1.fits
```

Appendix B

celldetect & deflare, visualization example

As introduced in 3.1, `celldetect` was used to detect point sources on the event files in order to exclude them when extracting the lightcurve. After excluding such point sources, the lightcurve is extracted with `dmextract` and the `deflare` routine is applied to the lightcurve to define GTI filters to cut time intervals of high flaring background.

`celldetect` creates a region file with ellipses enclosing the point sources, an example worked on the 2002 observation ObsID 3392 can be seen in figure B.1. The extracted lightcurve and its deflaring is in figure B.2.

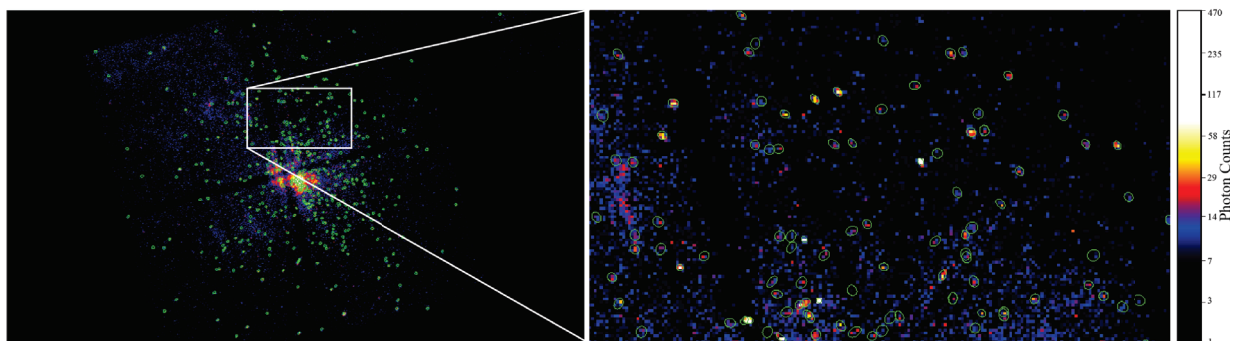


Figure B.1: *Left*: The counts image of the event file is shown, on top there are plotted the regions created with `celldetect`. *Right*: A closer look to a part of the counts image with the regions from `celldetect`, it can be seen that the regions enclose point sources, distinguished by the brighter coloring⁶⁶.

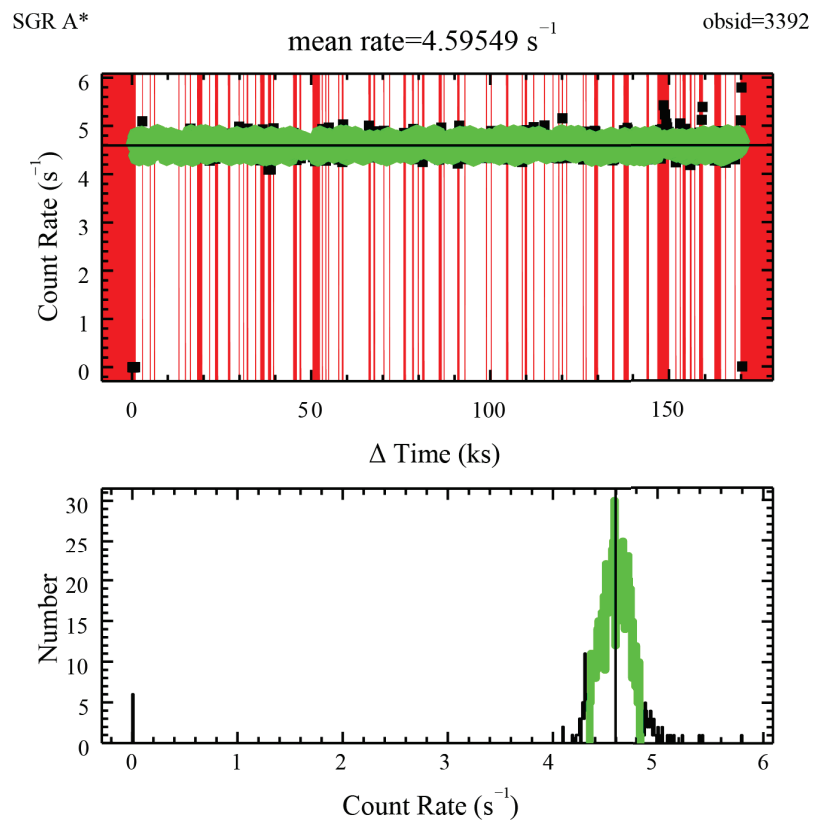


Figure B.2: *Top*: The lightcurve of the observation 3392 is plotted, the red regions represent the time intervals to be filtered out. *bottom*: A histogram of the count rate is shown, the black regions represent the events to be filtered out (events with count rate outside $\pm 2\sigma$ with respect to the mean)⁶⁶.

Bibliography

- [1] RONTGEN, W. C. ON A NEW KIND OF RAYS. *Science* **1896**, 3, 227–231.
- [2] PuluJ, J. *Strahlende Elektroden-Materie und der sogenannte vierte Aggregatzustand*; 1883.
- [3] Hanke, M. High-resolution X-ray Spectroscopy of the Black Hole Cygnus X-1 with the Chandra X-ray Observatory. Ph.D. thesis, Astronomical Institute of the University of Erlangen-Nuremberg, 2007.
- [4] DePasquale, J.; Arcand, K.; Edmonds, P. High Energy Vision: Processing X-rays. *Studies in Media and Communication* **2015**, 3.
- [5] Keith Arnaud, A. S., ParkRandall Smith, Ed. *Cambridge Observing Handbooks for Research Astronomers*; Cambridge University Press, 2011.
- [6] CXC, In *The Chandra Proposers' Observatory Guide*; Chandra Project Science, M. C. I. T., Ed.; Chandra XCenter, 2018.
- [7] Giacconi, R.; Gursky, H.; Speybroeck, L. P. V. Observational Techniques in X-Ray Astronomy. *Annual Review of Astronomy and Astrophysics* **1968**, 6, 373–416.
- [8] Charles, P.; Fabian, A. The new X-ray universe. *Astronomy and Geophysics* **2001**, 42, 611–616.
- [9] Koyama, K. *et al.* Iron and Nickel Line Diagnostics for the Galactic Center Diffuse Emission. *Publications of the Astronomical Society of Japan* **2007**,
- [10] Tatischeff, V.; Decourchelle, A.; Maurin, G. Nonthermal X-rays from low-energy cosmic rays: application to the 6.4 keV line emission from the Arches cluster region. *Astronomy & Astrophysics* **2012**, 546, A88.
- [11] Krause, M. O.; Oliver, J. H. Natural widths of atomic K and L levels, $K\alpha$ X-ray lines and several KLL Auger lines. *Journal of Physical and Chemical Reference Data* **1979**, 8, 329–338.
- [12] Genzel, R.; Eisenhauer, F.; Gillessen, S. The Galactic Center massive black hole and nuclear star cluster. *Reviews of Modern Physics* **2010**, 82, 3121–3195.

- [13] Eckart, A.; Hüttemann, A.; Kiefer, C.; Britzen, S.; Zajaček, M.; Lämmerzahl, C.; Stöckler, M.; Valencia-S, M.; Karas, V.; García-Marín, M. The Milky Way's Supermassive Black Hole: How Good a Case Is It? *Foundations of Physics* **2017**, *47*, 553–624.
- [14] Boyce, H.; Haggard, D.; Witzel, G.; Willner, S. P.; Neilsen, J.; Hora, J. L.; Markoff, S.; Ponti, G.; Baganoff, F.; Becklin, E. E.; Fazio, G. G.; Lowrance, P.; Morris, M. R.; Smith, H. A. Simultaneous X-Ray and Infrared Observations of Sagittarius A*'s Variability. *The Astrophysical Journal* **2019**, *871*, 161.
- [15] Mezger, P. G.; Duschl, W. J.; Zylka, R. The Galactic Center: a laboratory for AGN? *Astronomy and Astrophysics Review* **1996**, *7*, 289–388.
- [16] Genzel, R.; Hollenbach, D.; Townes, C. H. The nucleus of our Galaxy. *Reports on Progress in Physics* **1994**, *57*, 417–479.
- [17] Baganoff, F. K.; Bautz, M. W.; Brandt, W. N.; Chartas, G.; Feigelson, E. D.; Garmire, G. P.; Maeda, Y.; Morris, M.; Ricker, G. R.; Townsley, L. K.; Walter, F. Rapid X-ray flaring from the direction of the supermassive black hole at the Galactic Centre.
- [18] Baganoff, F. K.; Maeda, Y.; Morris, M.; Bautz, M. W.; Brandt, W. N.; Cui, W.; Doty, J. P.; Feigelson, E. D.; Garmire, G. P.; Pravdo, S. H.; Ricker, G. R.; Townsley, L. K. Chandra X-ray Spectroscopic Imaging of Sgr A* and the Central Parsec of the Galaxy.
- [19] Baganoff, F. K. Multiwavelength Monitoring of Sgr A* During Chandra Observations of Multiple X-ray Flares. 2003; <http://adsabs.harvard.edu/abs/2003HEAD...7.0302B>.
- [20] Munro, M. P.; Baganoff, F. K.; Bautz, M. W.; Feigelson, E. D.; Garmire, G. P.; Morris, M. R.; Park, S.; Ricker, G. R.; Townsley, L. K. Diffuse X-ray Emission in a Deep Chandra Image of the Galactic Center.
- [21] Lo, K. Y.; Claussen, M. J. High-resolution observations of ionized gas in central 3 parsecs of the Galaxy: possible evidence for infall. *Nature* **1983**, *306*, 647–651.
- [22] Guesten, R.; Genzel, R.; Wright, M. C. H.; Jaffe, D. T.; Stutzki, J.; Harris, A. I. Aperture synthesis observations of the circumnuclear ring in the Galactic center. *The Astrophysical Journal* **1987**, *318*, 124.
- [23] Becklin, E. E.; Gatley, I.; Werner, M. W. Far-infrared observations of Sagittarius A - The luminosity and dust density in the central parsec of the Galaxy. **1982**, *258*, 135–142.
- [24] Becklin, E. E.; Neugebauer, G. Infrared Observations of the Galactic Center. *The Astrophysical Journal* **1968**, *151*, 145.
- [25] Krichbaum, G. D. A. W. A. G. A. W. J. E. G. M., T. P. VLBI observations of the galactic center source SGR A* at 86 GHz and 215 GHz. *Astronomy and Astrophysics*, v.335, p.L106-L110 **1998**,

- [26] Rogers, A. E. E.; Doeleman, S.; Wright, M. C. H.; Bower, G. C.; Backer, D. C.; Padin, S.; Philips, J. A.; Emerson, D. T.; Greenhill, L.; Moran, J. M.; Kellermann, K. I. Small-scale structure and position of Sagittarius A(*) from VLBI at 3 millimeter wavelength. *1994*, *434*, L59–L62.
- [27] Shen, Z.-Q.; Lo, K. Y.; Liang, M.-C.; Ho, P. T. P.; Zhao, J.-H. A size of ~ 1 au for the radio source Sgr A* at the centre of the Milky Way. *Nature* **2005**, *438*, 62–64.
- [28] Doeleman, S. S.; Shen, Z.-Q.; Rogers, A. E. E.; Bower, G. C.; Wright, M. C. H.; Zhao, J. H.; Backer, D. C.; Crowley, J. W.; Freund, R. W.; Ho, P. T. P.; Lo, K. Y.; Woody, D. P. Structure of Sagittarius A* at 86 GHz using VLBI Closure Quantities. *The Astronomical Journal* **2001**, *121*, 2610–2617.
- [29] Zhang, S. Investigating the Physics of Hard X-ray Outbursts from the Galactic Center Supermassive Black Hole Sagittarius A*. Ph.D. thesis, COLUMBIA UNIVERSITY, 2016.
- [30] Koyama, K.; Maeda, Y.; Sonobe, T.; Takeshima, T.; Tanaka, Y.; Yamauchi, S. ASCA View of Our Galactic Center: Remains of Past Activities in X-Rays? *Publications of the Astronomical Society of Japan* **1996**, *48*, 249–255.
- [31] Sunyaev, R. A.; Markevitch, M.; Pavlinsky, M. The center of the Galaxy in the recent past - A view from GRANAT. *The Astrophysical Journal* **1993**, *407*, 606.
- [32] Munro, M. P.; Baganoff, F. K.; Brandt, W. N.; Park, S.; Morris, M. R. Discovery of Variable Iron Fluorescence from Reflection Nebulae in the Galactic Center. *The Astrophysical Journal* **2007**, *656*, L69–L72.
- [33] Koyama, K.; Takikawa, Y.; Hyodo, Y.; Inui, T.; Nobukawa, M.; Matsumoto, H.; Tsuru, T. G. Spatial Distribution of the Galactic Center Diffuse X-Rays and the Spectra of the Brightest 6.4 keV Clumps. *Publications of the Astronomical Society of Japan* **2009**, *61*, S255–S262.
- [34] Yuasa, T.; Ichi Tamura, K.; Nakazawa, K.; Kokubun, M.; Makishima, K.; Bamba, A.; Maeda, Y.; Takahashi, T.; Ebisawa, K.; Senda, A.; Hyodo, Y.; Tsuru, T. G.; Koyama, K.; Yamauchi, S.; Takahashi, H. Suzaku Detection of Extended/Diffuse Hard X-Ray Emission from the Galactic Center. *Publications of the Astronomical Society of Japan* **2008**, *60*, S207–S221.
- [35] Tanaka, Y. ASCA observation of X-ray emission from the Galactic ridge. *Astronomy & Astrophysics* **2002**, *382*, 1052–1060.
- [36] Krivonos, R.; Revnivtsev, M.; Lutovinov, A.; Sazonov, S.; Churazov, E.; Sunyaev, R. INTEGRAL/IBIS all-sky survey in hard X-rays. *Astronomy & Astrophysics* **2007**, *475*, 775–784.
- [37] Hailey, C. J. *et al.* Evidence for intermediate polars as the origin of the Galactic Center hard X-ray emission.
- [38] Revnivtsev, M.; Molokov, S.; Sazonov, S. Large-scale variations of the cosmic X-ray background and the X-ray emissivity of the local Universe. *Astronomy & Astrophysics* **2008**, *483*, 425–435.

- [39] Symposium, I. A. U.; Meurs, E.; Fabbiano, G. *Populations of High-Energy Sources in Galaxies (IAU S230)*; IAU Symposium; Cambridge University Press, 2006.
- [40] Freitag, M.; Amaro-Seoane, P.; Kalogera, V. Stellar Remnants in Galactic Nuclei: Mass Segregation. *The Astrophysical Journal* **2006**, *649*, 91–117.
- [41] Falcke, H.; Goss, W. M.; Matsuo, H.; Teuben, P.; Zhao, J.-H.; Zylka, R. The Simultaneous Spectrum of Sagittarius A* from 20 Centimeters to 1 Millimeter and the Nature of the Millimeter Excess. *The Astrophysical Journal* **1998**, *499*, 731–734.
- [42] Yusef-Zadeh, F.; Roberts, D.; Wardle, M.; Heinke, C. O.; Bower, G. C. Flaring Activity of Sagittarius A* at 43 and 22 GHz: Evidence for Expanding Hot Plasma. *The Astrophysical Journal* **2006**, *650*, 189–194.
- [43] Li, J.; Shen, Z.-Q.; Miyazaki, A.; Huang, L.; Sault, R. J.; Miyoshi, M.; Tsuboi, M.; Tsutsumi, T. THE VARIABILITY OF SAGITTARIUS A* AT 3 MILLIMETER. *The Astrophysical Journal* **2009**, *700*, 417–425.
- [44] Marrone, D. P. *et al.* An X-ray, IR, and Submillimeter Flare of Sagittarius A*.
- [45] Xu, Y.-D.; Narayan, R.; Quataert, E.; Yuan, F.; Baganoff, F. K. Thermal X-Ray Iron Line Emission from the Galactic Center Black Hole Sagittarius A*. *The Astrophysical Journal* **2006**, *640*, 319–326.
- [46] Narayan, R.; Yi, I.; Mahadevan, R. Explaining the spectrum of Sagittarius A* with a model of an accreting black hole. *Nature* **1995**, *374*, 623–625.
- [47] Ball, G. H.; Narayan, R.; Quataert, E. Spectral Models of Convection-dominated Accretion Flows. *The Astrophysical Journal* **2001**, *552*, 221–226.
- [48] Narayan, R.; Quataert, E.; Igumenshchev, I. V.; Abramowicz, M. A. The Magnetohydrodynamics of Convection-dominated Accretion Flows. *The Astrophysical Journal* **2002**, *577*, 295–301.
- [49] Quataert, E.; Gruzinov, A. Convection-dominated Accretion Flows. *The Astrophysical Journal* **2000**, *539*, 809–814.
- [50] Yuan, F.; Quataert, E.; Narayan, R. Nonthermal Electrons in Radiatively Inefficient Accretion Flow Models of Sagittarius A*. *The Astrophysical Journal* **2003**, *598*, 301–312.
- [51] Blandford, R. D.; Begelman, M. C. On the fate of gas accreting at a low rate on to a black hole. *Monthly Notices of the Royal Astronomical Society* **1999**, *303*, L1–L5.
- [52] Yuan, F.; Markoff, S.; Falcke, H. A Jet-ADAF model for Sgr A*. *Astronomy & Astrophysics* **2002**, *383*, 854–863.
- [53] Quataert, E. A Thermal Bremsstrahlung Model For the Quiescent X-ray Emission from Sagittarius A*.
- [54] Porquet, D.; Predehl, P.; Aschenbach, B.; Grosso, N.; Goldwurm, A.; Goldoni, P.; Warwick, R. S.; Decourchelle, A. XMM-Newton observation of the brightest X-ray flare detected so far from Sgr A*. *Astronomy & Astrophysics* **2003**, *407*, L17–L20.

- [55] Dodds-Eden, K. *et al.* EVIDENCE FOR X-RAY SYNCHROTRON EMISSION FROM SIMULTANEOUS MID-INFRARED TO X-RAY OBSERVATIONS OF A STRONG Sgr A* FLARE. *The Astrophysical Journal* **2009**, 698, 676–692.
- [56] Markoff, S.; Falcke, H.; Yuan, F.; Biermann, P. L. The Nature of the 10 kilosecond X-ray flare in Sgr A*. *Astronomy & Astrophysics* **2001**, 379, L13–L16.
- [57] Yusef-Zadeh, F.; Wardle, M.; Roy, S. Cosmic-Ray Heating of Molecular Gas in the Nuclear Disk: Low Star Formation Efficiency. *The Astrophysical Journal* **2007**, 665, L123–L126.
- [58] Eckart, A.; Baganoff, F. K.; Morris, M.; Bautz, M. W.; Brandt, W. N.; Garmire, G. P.; Genzel, R.; Ott, T.; Ricker, G. R.; Straubmeier, C.; Viehmann, T.; Schödel, R.; Bower, G. C.; Goldston, J. E. First simultaneous NIR/X-ray detection of a flare from Sgr A*. *Astronomy & Astrophysics* **2004**, 427, 1–11.
- [59] Yuan, F. Accretion and ejection in Sgr A*.
- [60] Sharma, P.; Quataert, E.; Hammett, G. W.; Stone, J. M. Electron Heating in Hot Accretion Flows. *The Astrophysical Journal* **2007**, 667, 714–723.
- [61] Hawley, J. F.; Balbus, S. A. The Dynamical Structure of Nonradiative Black Hole Accretion Flows. *The Astrophysical Journal* **2002**, 573, 738–748.
- [62] Mościbrodzka, M.; Gammie, C. F.; Dolence, J. C.; Shiokawa, H.; Leung, P. K. RADIATIVE MODELS OF SGR A* FROM GRMHD SIMULATIONS. *The Astrophysical Journal* **2009**, 706, 497–507.
- [63] Wolter, H. Verallgemeinerte Schwarzschildsche Spiegelsysteme streifender Reflexion als Optiken für Röntgenstrahlen. *Annalen der Physik* **1952**, 445, 286–295.
- [64] Clavel, M.; Terrier, R.; Goldwurm, A.; Morris, M. R.; Ponti, G.; Soldi, S.; Trap, G. Echoes of multiple outbursts of Sagittarius A* revealed by Chandra. *Astronomy & Astrophysics* **2013**, 558, A32.
- [65] Ponti, G.; Terrier, R.; Goldwurm, A.; Belanger, G.; Trap, G. DISCOVERY OF A SUPERLUMINAL Fe K ECHO AT THE GALACTIC CENTER: THE GLORIOUS PAST OF Sgr A* PRESERVED BY MOLECULAR CLOUDS. *The Astrophysical Journal* **2010**, 714, 732–747.
- [66] Fruscione, A. *et al.* CIAO: Chandra's data analysis system. 2006.
- [67] Joye, W. A.; Mandel, E. New Features of SAOImage DS9. 2003; <http://adsabs.harvard.edu/abs/2003ASPC..295..489J>.
- [68] Freeman, P.; Doe, S.; Siemiginowska, A. Sherpa: a mission-independent data analysis application. 2001.
- [69] Wells, D. C.; Greisen, E. W.; Harten, R. H. FITS - a Flexible Image Transport System. **1981**, 44, 363.

- [70] Li, J.; Kastner, J. H.; Prigozhin, G. Y.; Schulz, N. S.; Feigelson, E. D.; Getman, K. V. ChandraACIS Subpixel Event Repositioning: Further Refinements and Comparison between Backside- and Frontside-illuminated X-Ray CCDs. *The Astrophysical Journal* **2004**, *610*, 1204–1212.
- [71] Keith Arnaud, C. G. . B. D. Xspec, An X-Ray Spectral Fitting Package, Users' Guide for version 12.10.1. 2018.
- [72] Moré, J. J. *Lecture Notes in Mathematics*; Springer Berlin Heidelberg, 1978; pp 105–116.
- [73] Capelli, R.; Warwick, R. S.; Porquet, D.; Gillessen, S.; Predehl, P. The X-ray lightcurve of Sagittarius A* over the past 150 years inferred from Fe-K α line reverberation in Galactic centre molecular clouds. *Astronomy & Astrophysics* **2012**, *545*, A35.
- [74] Nobukawa, M.; Koyama, K.; Tsuru, T. G.; Ryu, S. G.; Tatischeff, V. Discovery of K-Shell Emission Lines of Neutral Atoms in the Galactic Center Region. *Publications of the Astronomical Society of Japan* **2010**, *62*, 423–429.
- [75] George, I. M.; Fabian, A. C. X-ray reflection from cold matter in Active Galactic Nuclei and X-ray binaries. *Monthly Notices of the Royal Astronomical Society* **1991**, *249*, 352–367.
- [76] Yusef-Zadeh, F.; Law, C.; Wardle, M. The Origin of X-Ray Emission from a Galactic Center Molecular Cloud: Low-Energy Cosmic-Ray Electrons. *The Astrophysical Journal* **2002**, *568*, L121–L125.
- [77] Dogiel, V. A.; Tatischeff, V.; Cheng, K. S.; Chernyshov, D. O.; Ko, C. M.; Ip, W. H. Nuclear interaction gamma-ray lines from the Galactic center region. *Astronomy & Astrophysics* **2009**, *508*, 1–7.
- [78] Dogiel, V.; Chernyshov, D.; Koyama, K.; Nobukawa, M.; Cheng, K.-S. K-Shell Emission of Neutral Iron Line from Sagittarius B2 Excited by Subrelativistic Protons. *Publications of the Astronomical Society of Japan* **2011**, *63*, 535–541.